Chemical Engineering Science 139 (2016) 75–98

Contents lists available at ScienceDirect

Chemical Engineering Science

journal homepage: www.elsevier.com/locate/ces

Coupled multiphase transport, large deformation and phase transition during rice puffing

Tushar Gulati, Ashim K. Datta *

Department of Biological and Environmental Engineering, Cornell University, 208 Riley Robb Hall, Ithaca, NY-14853, USA

HIGHLIGHTS

- A framework for transport and deformation is presented for puffing-type processes.
- Rubbery/glassy phase transition is a critical component for puffing-type processes.
- Large gas pressure generation and glass-to-rubber phase transition cause puffing.
- Salt-assisted and gun puffing of rice are explained in a fundamental way.

ARTICLE INFO

Article history:
Received 28 April 2015
Received in revised form
23 August 2015
Accepted 30 August 2015
Available online 18 September 2015

Keywords:
Rice
Salt-assisted puffing
Gun-puffing
Large deformation
Multiphase modeling
Porous media

ABSTRACT

Puffing of biomaterials involves mass, momentum and energy transport along with large volumetric expansion of the material. Development of fundamentals-based models that can describe heat and moisture transport, rapid evaporation and large deformations can help understand the factors affecting the puffing processes and optimize them. In this context, salt-assisted puffing of parboiled rice is described. A multiphase porous media model involving heat and mass transfer within the rice kernel undergoing large deformations is developed. The transport model involves different phases and multiple modes of transport. During puffing, intensive heating of rice leads to rapid evaporation of water to vapor resulting in large pressure development. Also, the rice starch undergoes Glass Transition from a rigid, glassy state to a soft, rubbery state. Development of large pressures within a soft matrix results in large volumetric expansion of the kernel causing it to puff. The developed model was validated against moisture changes and volumetric expansion of the rice kernel during the puffing process and good agreement was found. Gas porosity development in puffed rice was determined via 3D reconstruction of micro-CT images of rice puffed at different times which compared favorably well with model predictions. The expansion of the kernel began from the tip of the grain and the model could successfully capture this phenomenon. Expansion ratio, a key quality parameter associated with puffed products, was found to be sensitive to intrinsic permeability and bulk modulus of the solid matrix. The modeling framework for salt-assisted puffing was then extended to the process of gun-puffing (a completely different puffing process) without significant reformulations thus showing the applicability of the framework for a variety of puffing processes. The final expansion after gun-puffing was much higher compared with salt-assisted puffing and was found to be sensitive to the gun opening time.

1. Introduction

Cereal grains, e.g., corn, wheat, rice, oats, are widely processed for ready-to-eat-breakfast cereals, infant foods and snack foods (Maisont and Narkrugsa, 2010). One of the many ways in which grains are processed is by puffing. For example, corn has been widely used to make the popular puffed snack popcorn and breakfast cereal cornflakes (Hoseney et al., 1983). Rice has been consumed as a staple food for centuries. In many South-Asian countries, puffed rice is famously consumed as a light snack food in different forms like puffed rice balls and cakes (Simsrisakul, 1991). There is growing consumer interests towards puffed foods and snacks as they are healthy, low in fat, and bear quite a resemblance to the crispy texture of fried foods (Moraru and Kokini, 2006).

Puffing of cereals and starch based foods have been carried out using a variety of techniques, e.g. using hot oil (Villareal and Juliano, 1987), gun-puffing (Villareal and Juliano, 1987), sand or

* Corresponding author. Tel.: +1 607 255 2482.
E-mail address: akd1@cornell.edu (A.K. Datta).

http://dx.doi.org/10.1016/j.ces.2015.08.057
0009-2509/

salt-assisted (Chinnaswamy and Bhattacharya, 1983; Hoke et al., 2007), hot-air (Guraya and Toledo, 1994; Varnalis et al., 2004; Nath et al., 2007; Norton et al., 2011), microwaves (Maisont and Narkrugsa, 2010; Rakesh and Datta, 2011; Joshi et al., 2014) and extrusion (Lue et al., 1991; Moraru and Kokini, 2006; Moscicki, 2011). In all these different processes, the material is subjected to very high temperatures resulting in "flash off" of liquid water to vapor. This sudden evaporation leads to pressure generation within the materials causing them to puff. The volumetric expansion ratio (i.e., the ratio of initial to final volume) of the puffed material could lie anywhere between 4 and 10 (Chandrashekhar and Chattopadhyay, 1991). From a quality standpoint, the higher the expansion ratio, the better is the quality of the puffed product. In order to obtain better quality products, a good understanding of the underlying mechanisms involved in the expansion process is needed through physics-based modeling and detailed experimentation. The present work aims toward developing a fundamentals-based model in order to understand puffing processes and apply the framework to study salt-assisted and gun-puffing of rice kernels. Although the model presented here is for rice puffing, the physics of the process is quite similar to other puffing processes and can be extended to understand and optimize those processes as well. Moreover, the manufacturing of foamed plastics, e.g., polystyrene, is quite similar during which a gas generating substance (i.e., blowing agent) is introduced into a molten polymer at elevated pressures. By suddenly reducing the surrounding temperature and pressure, expansion of the gas phase inside the polymer melt takes place, eventually causing them to puff (Arefmanesh et al., 1990; Elshereef et al., 2010). The framework developed here can be applied as well to foam forming processes that is of prime importance in the chemical process industry.

Rice puffing using different techniques has primarily been studied in the context of obtaining optimum processing conditions that would yield a product with a high expansion ratio (Hoke et al., 2005). Preprocessing of rice before puffing is a crucial step in order to obtain good quality puffed rice. Initial moisture content, puffing temperatures and degree of salt addition in the preprocessing steps are some of the most critical factors that favor large volumes of the puffed product. Studies have shown that an initial moisture content of rice kernels ranging between 10% and 15% (wet basis) and pre-gelatinization of rice starch have resulted in better quality puffed rice obtained using different intense heating processes (Chinnaswamy and Bhattacharya, 1983; Murugesan and Bhattacharya, 1991; Villareal and Juliano, 1987; Simsrisakul, 1991; Maisont and Narkrugsa, 2010). Starch is the prime component of rice and many other cereal grains. In its native crystalline form, starch does not allow for a large expansion of the kernel because when heated, starch reacts with water to undergo gelatinization (van der Sman and Broeze, 2013). This reduces the amount of water available for vapor generation during the puffing process. Rice is therefore pretreated before puffing by soaking it in water overnight followed by drying between 70–90 °C and 10–15% moisture content (wet basis) (Mohapatra et al., 2012). In the pretreatment process, starch and excess water undergo gelatinization during which starch molecules lose their crystallinity and become amorphous (Briffaz et al., 2012). Once starch loses its native form, it does not react with water during the puffing stage (van der Sman and Meinders, 2011). Therefore, with sufficient water available to generate vapors, a product with a high expansion ratio is achieved when compared with untreated rice (Chinnaswamy and Bhattacharya, 1983). Also, pre-gelatinized starch provides a crunchy texture to the puffed product (Willard, 1976).

After pre-treatment, rice kernels are subjected to intense heat for puffing. Initially, the starch in rice is in the glassy state, i.e., it is hard and rigid. During the heating step, two things happen: (1) moisture inside the rice grains starts to evaporate resulting in the formation of vapors, and (2) rice starch undergoes a phase transformation from the hard, glassy state to the soft, rubbery state. Due to intense vapor generation, large pressures are generated within the kernel in a soft and compliant matrix due to glassy–rubbery phase transformation. As a result, the matrix undergoes large expansion consequently releasing the gas pressure in this process. The end of rice puffing is marked by a distinct popping sound (Murugesan and Bhattacharya, 1991).

1.1. Mathematical modeling of puffing-type processes

Puffing of food materials involves mass, momentum and energy transport along with large volumetric expansion of a porous, thermoplastic material (Rakesh and Datta, 2011; Kong and Shanks, 2012). Mathematical models of puffing-type processes have primarily focused on understanding how a microscopic single vapor bubble grows in a pool of molten starch (bubble growth models). Some examples include modeling bubble growth during proving and baking of bread dough (Shah et al., 1998; Fan et al., 1999; Chiotellis and Campbell, 2003; Hailemariam et al., 2007; Deshlahra et al., 2009), vapor induced puffing of corn (Schwartzberg et al., 1995), extrusion cooking of starch (Kokini et al., 1992; Fan et al., 1994; Wang et al., 2005) and supercritical fluid extrusion (Alavi et al., 2003a,b). These models have ignored transport phenomena at the macroscale with one notable exception as shown by Alavi et al. (2003a,b). However, the model used effective diffusivity formulations and did not take into account the pressure driven flow and distributed evaporation that are critical to puffing type processes. Furthermore, in all of the above models, water vapor is assumed to be in equilibrium with liquid water which is not true for intense heating processes (discussed later).

Puffing involves a two-way coupling of transport phenomena and non-linear solid mechanics (Zhang et al., 2005; Rakesh and Datta, 2012; Nicolas et al., 2014) to be able to accurately describe the process. The transport phenomena involve multiple phases with multiple modes of transport and phase change inside a material that undergoes large inelastic deformations. Macroscopic models that include the detailed physics of the process can provide for an integrated understanding of how a material structure, e.g., porosity, develops as a whole that can ultimately be related to quality of the final puffed product. Models that account for transport and deformation have been developed for various other applications. Of them, most have assumed small deformations that are generally not true and are definitely not applicable to the process of rice puffing. Others have simplified transport models that do not take into account the different phases and modes of transport (Achanta, 1995; Shi et al., 1998; Yang et al., 2001; Mayor and Sereno, 2004; Katekawa and Silva, 2006; Ressing et al., 2007; Niamnuy et al., 2008; Perez et al., 2012). More recently, detailed models including transport with large deformations have been developed; however, the models assume constant mechanical properties and do not account for glassy–rubbery phase transformation that is important for puffing-type processes (Rakesh and Datta, 2011).

1.2. Objectives and overview

Therefore, the overarching goal of this study is to develop a general framework for puffing of biomaterials that can take into account a variety of features that are specific to puffing-type processes, using rice puffing as an example. The organization of the work is as follows: the coupled transport and large deformation model for puffing is described first. This is followed by experimental methodology undertaken to perform the puffing experiments on rice kernels and measurement of moisture

content, volume and expansion ratio, porosity development in the puffed product to validate the computational model and understand the puffing process. The model is then used to study the effect of different processing conditions on the final quality of the puffed product. This is followed by a parametric sensitivity analysis of some key parameters carried out to study the effects of their variability as affecting final volume of the puffed product. Finally, the modeling framework for salt-assisted puffing is extended to the process of gun-puffing (a completely different puffing process) to show the applicability of the framework for other puffing-type processes.

2. Model development

In this section, a porous media based multiphase, multicomponent model coupled with large deformations of the elasto-plastic solid matrix is presented to mathematically describe puffing of rice grains in a high-temperature bed. Major assumptions, governing equations, initial and boundary conditions, along with auxiliary conditions, are described. The two different physics, i.e., transport and solid mechanics, are fully coupled since transport processes result in pressure generation that causes the material to greatly deform while deformation affects transport through significantly changed geometry and transport properties (porosity and permeability) (see Fig. 1).

2.1. A qualitative description of the process

A number of simplifying assumptions are needed to mathematically describe the rice puffing process. The material is treated as a continuum that comprises three phases – solid matrix, liquid water and the gas phase (water vapor and air). Using spatial averaging techniques defined over a Representative Elementary Volume (REV), macroscopic equations for conservation of mass, momentum and energy are defined. The solid phase composed of pre-gelatinized starch undergoes a phase transformation from the initial hard glassy state to the soft rubbery state when subjected to high temperatures. Furthermore, it is considered isotropic and elasto-plastically deformable. The pore space is composed of liquid water and gas (air and water vapor) with the gas phase assumed to follow ideal gas law. The porosity (pore space) is defined as the volume occupied by all the fluid phases. This is different from the conventional definition of porosity which is defined as the volume occupied by the gas phase only. It is assumed that all of the starch is present in its amorphous state and, therefore, all the liquid water is available for vapor generation; starch gelatinization, if any, is assumed small and neglected. Interphase mass transfer occurs between liquid water and vapor in gas phase due to evaporation. For such intense heating processes, non-equilibrium can potentially exist between liquid water and water vapor (Halder et al., 2007) and, therefore, vapor concentrations at a location are close to that given by moisture isotherms but not necessarily the same. Vapor generation due to intense evaporation leads to pressure development that deforms the solid. This changes its structure (porosity) and in turn liquid and gas permeabilities of the matrix. Changes in geometry, porosity and permeabilities affect transport and, therefore, the problem is two-way coupled. Local thermal equilibrium is assumed among the different phases inside the material so all phases share the same temperature at a location. The effect of gravity on mass transport is ignored since moisture fluxes due to pressure gradients are quite large.

2.2. Solid mechanics

Deformation during puffing is caused by intense internal evaporation of liquid water to vapor resulting in large pressure generation. The material undergoes large elastic and inelastic deformations, thereby expanding in this process. Since the material is porous and undergoes large, permanent changes in its volume and structure, it is assumed to behave as a porohyperelastic – perfectly plastic solid. The material continuum is expressed mathematically in terms of the volume of solid and fluid phases as shown in Fig. 2:

$$\Delta V = \Delta V_s + \Delta V_f \tag{1}$$

where s and f stand for the solid and fluid phases, respectively, and V is the total volume of the material. Inside a Representative Elementary Volume (REV), the fraction of volume occupied by the

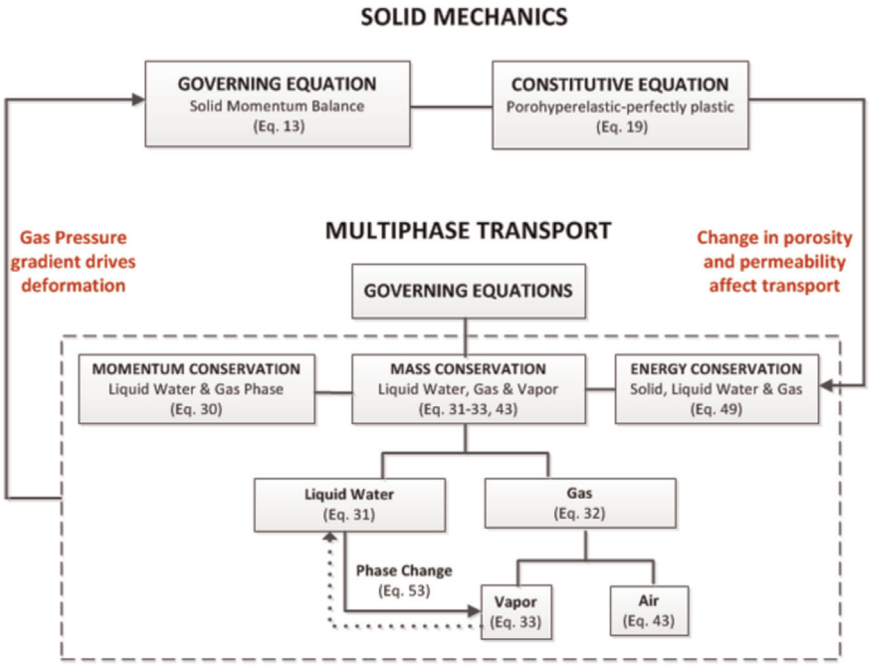

Fig. 1. Flowchart showing the two-way coupling between poromechanics and multiphase transport during rice puffing.

fluid phases is defined in terms of porosity, ϕ, as

$$\phi = \frac{\Delta V_f}{\Delta V} = \frac{\Delta V_w + \Delta V_g}{\Delta V} \tag{2}$$

where w and g stand for the liquid water and gas phases, respectively. Individually, both solid and fluid phases are incompressible; however, the material as a whole is compressible as there is a net change in the concentration of gas phase during puffing. This is responsible for porosity development during the puffing process. At any instant of time, t, ϕ in a deforming material can be obtained by conserving the volume of the solid phase as

$$(1-\phi(t))\Delta V = (1-\phi_0)\Delta V_0 \tag{3}$$

$$\phi(t) = 1-(1-\phi_0)\frac{\Delta V_0}{\Delta V} \tag{4}$$

$$\phi(t) = 1-\frac{(1-\phi_0)}{J} \tag{5}$$

The ratio of the final to initial volume of the material is denoted by Jacobian, J, which is obtained as the determinant of deformation gradient tensor, **F**. The deformation gradient tensor is a second order tensor that maps the displacements of the material in the deformed geometry (spatial frame) to that in the undeformed geometry (reference frame) as shown schematically in Fig. 3. In Lagrangian description of motion, the coordinates of spatial frame, $\overline{x}$, is a function of the coordinates in the material frame, $\overline{X}$, and current time t:

$$\overline{x} = \boldsymbol{\chi}(\overline{X}, t) \tag{6}$$

The displacement of a material point from $\overline{X}$ to $\overline{x}$ is defined in terms of a displacement vector, $\overline{u}$, as

$$\overline{u}(\overline{X}, t) = \boldsymbol{\chi}(\overline{X}, t) - \overline{X} \tag{7}$$

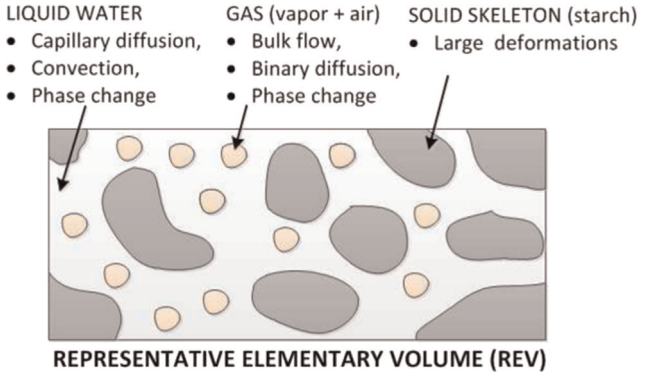

Fig. 2. Representative elementary volume showing the different phases and their transport modes.

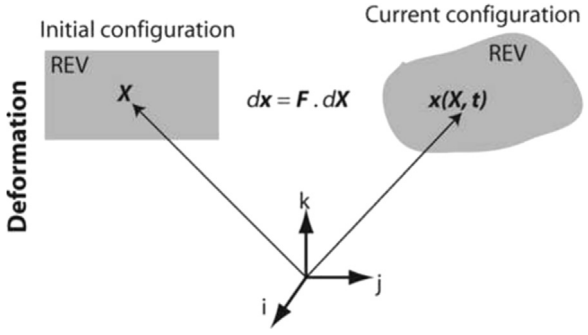

Fig. 3. Material and spatial configuration of the REV during puffing.

The deformation gradient, **F**, and the Jacobian, J, are then defined as

$$\mathbf{F} = \overline{\nabla}_X \cdot \overline{x} = \overline{\nabla}_X \cdot (\boldsymbol{\chi}(\overline{X}, t)) \tag{8}$$

$$J = \det(\mathbf{F}) \tag{9}$$

2.2.1. Conservation of linear momentum

Conservation of linear momentum solves for the stresses that generate inside the material during the puffing process. Since the material undergoes large deformation, Lagrangian measures of stresses and strains are used. The total stress acting on the material at any point inside the REV is the sum total of effective stress due to the solid skeleton and the pressures exerted by the fluid phases shown as

$$\overline{\boldsymbol{\sigma}}_{total} = \overline{\boldsymbol{\sigma}}_{eff} - p_f \mathbf{I} \tag{10}$$

The fluid pressure, p_f, is the volume averaged pressures exerted by the liquid water and gas phase, respectively, as

$$p_f = S_w p_w + S_g p_g \tag{11}$$

Assuming quasi-static loading conditions, the solid momentum balance on the material results in a divergence free stress state:

$$\overline{\nabla} \cdot \overline{\boldsymbol{\sigma}}_{total} = 0 \tag{12}$$

which implies that the divergence of effective stress on the solid skeleton is equal to the gradient of fluid pressure:

$$\overline{\nabla} \cdot \overline{\boldsymbol{\sigma}}_{eff} = \nabla p_f \tag{13}$$

Now, for intense heating processes, the contribution to total stress from the fluid phase is primarily due to gas pressure generation. Stresses due to moisture loss are assumed small and are neglected (Rakesh and Datta, 2011; Dhall and Datta, 2011). This is justified because during the puffing process, almost all of the water changes to vapor and the contribution to total stress by liquid water is negligible. Thus, we can write

$$\overline{\nabla} \cdot \overline{\boldsymbol{\sigma}}_{eff} = \nabla p_g \tag{14}$$

The effective stress in the solid skeleton is defined in the Lagrangian coordinate system in terms of the 2nd Piola–Kirchoff stress (PK2), **S**, as

$$\overline{\boldsymbol{\sigma}}_{eff} = J^{-1}\mathbf{F} \cdot \mathbf{S} \cdot \mathbf{F}^{\mathbf{T}} \tag{15}$$

2.2.2. Constitutive law

The material undergoes large deformations during the puffing process that are far beyond the elastic limit of starch molecules constituting the solid skeleton. Therefore, assuming an elastic, Hookean behavior (valid for small deformations) for the deforming solid would make the formulation inconsistent. Hooke's law is valid for a very small class of problems that involve small deformations only. Starch molecules have been found to exhibit elastic behavior at low stresses and plastic (flow) behavior at high stresses (Schwartzberg et al., 1995). Plastic deformations in starch occur primarily due to network elongation beyond a threshold stress limit defined as the yield stress (Genovese and Rao, 2003). The yield stress, therefore, marks the transition from elastic to plastic deformations. Based on these, for the present problem, the solid skeleton is modeled as a non-linearly elastic (hyperelastic) perfectly plastic solid.

2.2.3. Multiplicative split of deformation gradient

For an elasto-plastic material undergoing finite deformations, the material strain is based on the multiplicative split of the total deformation gradient tensor, **F**, into elastic, $\mathbf{F}_{el}$, and plastic

(inelastic), $\mathbf{F}_p$, components (Lewis and Shrefler, 1987):

$$\mathbf{F} = \mathbf{F}_{el}\mathbf{F}_p \tag{16}$$

In order to calculate elastic strains, the plastic deformation is removed from the total deformation gradient as

$$\mathbf{F}_{el} = \mathbf{F}\mathbf{F}_p^{-1} \tag{17}$$

As for stresses in the reference frame, Lagrangian measures of strains are used. The total strain is composed of an elastic and a plastic component. The elastic and plastic strains, $\mathbf{E}_{el}$ and $\mathbf{E}_p$, respectively, are defined in terms of their corresponding Right Cauchy Green deformation tensor, $\mathbf{C}_{el}$ and $\mathbf{C}_p$, respectively, as (Lewis and Shrefler, 1987)

$$\mathbf{E}_{el} = \tfrac{1}{2}(\mathbf{C}_{el} - \mathbf{I}) \tag{18}$$

$$\mathbf{E}_p = \tfrac{1}{2}(\mathbf{C}_p - \mathbf{I}) \tag{19}$$

where $\mathbf{C}_i = \mathbf{F}_i^T\mathbf{F}_i$ (i=el, p) and $\mathbf{I}$ is the identity tensor. The elastic component is assumed hyperelastic as noted above. For hyperelastic materials, a strain energy function, $W_s = W_s(\overline{\mathbf{C}}_{el}, \alpha)$, is defined that provides for the stress–strain relationship for the deforming solid. Here, $\overline{\mathbf{C}}_{el}$ is the deviatoric contribution of the elastic Right Cauchy Green deformation tensor, $\mathbf{C}_{el}$, and α is the effective plastic strain that is essentially an internal variable in the strain energy function. A two parameter Mooney–Rivlin material model is assumed for the present problem based on the strain levels the material experiences. The two parameter Mooney–Rivlin model can accommodate elastic strains up to 200% (Kim et al., 2012). This is indeed the case during rice puffing in which the material experiences elastic strains in the tune of 100% as will be shown in Section 5.6.1. The strain energy function is written in terms of the two isochoric invariants of the elastic Right Cauchy Green deformation tensor, $\overline{\mathbf{C}}_{el}$, and J (Holzapfel, 2000):

$$W_s = C_{01}\left[\bar{I}_1(\overline{\mathbf{C}}_{el}) - 3\right] + C_{10}\left[\bar{I}_2(\overline{\mathbf{C}}_{el}) - 3\right] + \tfrac{1}{2}\kappa[J-1] \tag{20}$$

where C_{01} and C_{10} are material constants that are related to the shear modulus, $G = 2(C_{01} + C_{10})$ with $C_{10} = 7C_{01}$ (Holzapfel, 2000), and K is the bulk modulus of the material. The first two terms in (20) constitute the isochoric or deviatoric part of the strain energy and the third term accounts for any volumetric changes that the material undergoes due to deformation from gas pressure gradients. The second law of thermodynamics yields the constitutive relation between Lagrangian (PK2) stresses and strains and the relationship between conjugate plastic internal variables q and α (Simo and Hughes, 1998):

$$\mathbf{S} = \frac{\partial W_s}{\partial \mathbf{E}_{el}} \tag{21}$$

$$q = -\frac{\partial W_s}{\partial \alpha} \tag{22}$$

For finite strain plasticity, a plastic flow rule and a hardening law are needed to describe the condition under which plastic deformations would occur. The associated flow rule is obtained by taking the Lie derivative of the left elastic Cauchy–Green deformation tensor, $\mathbf{B}_{el}$:

$$-\frac{1}{2}L(\mathbf{B}_{el}) = \lambda\frac{\partial F}{\partial \boldsymbol{\tau}} \tag{23}$$

$$\dot{\alpha} = \lambda\frac{\partial F}{\partial q} \tag{24}$$

together with the Kuhn–Tucker loading/unloading conditions for the plastic multiplier, λ, and the yield function, F:

$$\lambda \geq 0; \quad F = F(\boldsymbol{\tau}, T, M) \leq 0; \quad \lambda F = 0; \tag{25}$$

The Lie derivative of $\mathbf{B}_{el}$ is defined in terms of the right plastic Cauchy–Green rate, $\dot{\mathbf{C}}_p$, for a more consistent formulation:

$$L(\mathbf{B}_{el}) = \mathbf{F}\cdot\dot{\mathbf{C}}_p^{-1}\cdot\mathbf{F}^T \tag{26}$$

The yield function, F, is a second order surface in the stress space that depends upon the Kirchoff stress ($\boldsymbol{\tau}$), temperature (T) and moisture (M) of the material. Temperature and moisture play a role only through the yielding conditions, e.g., the yield stress of a material could be a function of temperature or moisture or both. For the present work, the material is assumed perfectly plastic, i.e., without any strain hardening as there is no data available on its strain hardening properties. The yield surface, therefore, does not include any strain terms:

$$F(\boldsymbol{s}, T, M) = \|\boldsymbol{s}\| - \sigma_0(T, M) \tag{27}$$

In Eq. (27) above, $\|\boldsymbol{s}\|$ is the L_2 norm of the Kirchoff stress deviator ($\boldsymbol{\tau}$) and σ_0 is the yield stress of the material as a function of temperature and moisture content. Eq. (27) is known as the von-Mises yield criterion. The set of Eqs. (23)–(27) solves for the plastic deformation gradient, $\mathbf{F}_p$. In finite elasto-plasticity theory, the elastic and plastic strains are not additive and are related to the total strain, $\mathbf{E}$, by means of the plastic deformation gradient, $\mathbf{F}_p$:

$$\mathbf{E}_{el} = \mathbf{F}_p^{-T}(\mathbf{E} - \mathbf{E}_p)\mathbf{F}_p^{-1} \tag{28}$$

Once the total strain is known, it can be expressed in terms of the total displacement that the material undergoes:

$$\mathbf{E} = \tfrac{1}{2}\left[(\overline{\nabla}_X\cdot\overline{u}) + (\overline{\nabla}_X\cdot\overline{u})^T + (\overline{\nabla}_X\cdot\overline{u})(\overline{\nabla}_X\cdot\overline{u})^T\right] \tag{29}$$

In a deforming medium, the flux of various other fluid phases are defined with respect to the moving solid (discussed later). With the displacements known from Eq. (29), the solid velocity, $\overline{v}_s$, can be computed accordingly:

$$\overline{v}_s = \frac{d\overline{u}}{dt} \tag{30}$$

2.3. Multiphase multicomponent transport in porous media

In this section, the governing equations for transport (momentum, mass and energy conservation) are described for the different phases (solid, liquid water, water vapor and air) that exist in the system.

2.3.1. Momentum conservation

For transport in porous media, Darcy's law is used to describe the flow of fluid phases. For a deforming material, the velocity of the fluid phase, $\overline{v}_{i,s}$, is obtained relative to the velocity of the solid matrix, $\overline{v}_s$ (see Eq. (30)), and is given by

$$v_{i,s} = -\frac{k_i k_{r,i}}{\mu_i}\nabla p_i \tag{31}$$

where $i=w, g, v$ denotes the liquid water, gas and vapor phases, respectively. The components of a phase (water vapor and air for gas) share the same velocity. The gas pressure, p_g, is given by the sum of partial pressures exerted by water vapor and air based on ideal gas law and is calculated by solving the overall mass balance equation of the gas phase (Eq. (33)).

2.3.2. Mass conservation

Mass conservation equations for liquid water, gas and water vapor are given by

$$\frac{\partial c_w}{\partial t} + \overline{\nabla}\cdot\overline{n}_{w,G} = -\dot{I} \tag{32}$$

$$\frac{\partial c_g}{\partial t} + \overline{\nabla}\cdot\overline{n}_{g,G} = \dot{I} \tag{33}$$

$$\frac{\partial(c_g\omega_v)}{\partial t}+\overline{\nabla}\cdot\overline{n}_{v,G}=\dot{I} \tag{34}$$

where $\dot{I}$ is the rate of evaporation of water to vapor. The mass conservation equations above solve for the respective volumetric concentrations, c_w and c_g, that are related to their relative saturations:

$$S_i=\frac{\Delta V_i}{\Delta V_f}=\frac{\Delta V_i}{\phi\Delta V},\quad i=w,g \tag{35}$$

i.e., $c_w=\rho_w S_w\phi$ and $c_g=\rho_g S_g\phi$. Since the solid matrix deforms, the flux of the fluid phases as perceived by a stationary observer on the ground is obtained by combining the flux arising due to solid movement to the flux of the fluid phases relative to the solid:

$$\underbrace{\overline{n}_{i,G}}_{\text{Flux relative to ground frame}}=\underbrace{\overline{n}_{i,s}}_{\text{Flux relative to deforming solid}}+\underbrace{c_i\overline{v}_s}_{\text{Additional flux due to solid movement}} \tag{36}$$

2.3.3. Mass fluxes

The flux of the liquid phase is in terms of net pressure acting on it. In addition to gas pressure, liquid water inside pores experience capillary pressure that is attractive in nature. Therefore, the net pressure acting on the liquid phase is given by

$$p_w=p_g-p_c \tag{37}$$

and the net flux relative to the solid phase is given by

$$\overline{n}_{w,s}=-\rho_w\frac{k_w k_{r,w}}{\mu_w}\nabla p_w \tag{38}$$

$$\overline{n}_{w,s}=-\rho_w\frac{k_w k_{r,w}}{\mu_w}\nabla(p_g-p_c) \tag{39}$$

$$\overline{n}_{w,s}=-\rho_w\frac{k_w k_{r,w}}{\mu_w}\nabla p_g+\rho_w\frac{k_w k_{r,w}}{\mu_w}\nabla p_c \tag{40}$$

$$\overline{n}_{w,s}=\rho_w\overline{v}_{w,s}+\rho_w\frac{k_w k_{r,w}}{\mu_w}\frac{\partial p_c}{\partial c_w}\nabla c_w \tag{41}$$

Eq. (41) can be written in terms of capillary diffusivity, $D_{w,cap}=-\frac{\partial p_c}{\partial c_w}\nabla c_w$, as

$$\overline{n}_{w,s}=\rho_w\overline{v}_{w,s}-D_{w,cap}\nabla c_w \tag{42}$$

The gas phase is composed of a binary mixture of water vapor and air. Based on Darcy's law, the flux of the gas phase is given by

$$\overline{n}_{g,s}=-\rho_g\frac{k_g k_{g,r}}{\mu_g}\nabla p_g \tag{43}$$

The concentrations of vapor and air are obtained by solving for their respective mass fractions, ω_v and ω_a. The vapor and air concentrations are related to gas concentration by their respective mass fraction, i.e. $c_v=\omega_v c_g$ and $c_a=\omega_a c_g$. Since gas is assumed as a binary mixture, the mass fraction of air is obtained via closure equations:

$$\omega_a=1-\omega_v \tag{44}$$

The mass flux of water vapor arises due to bulk flow (due to gas pressure gradient) and binary diffusion with air (Bird et al., 2001):

$$\overline{n}_{v,s}=-\rho_v\frac{k_g k_{g,r}}{\mu_g}\nabla p_g-\left(\frac{C_g^2}{\rho_g}\right)M_v M_a D_{bin}\nabla x_v \tag{45}$$

$$\overline{n}_{v,s}=\rho_v\overline{v}_{g,s}-\left(\frac{C_g^2}{\rho_g}\right)M_v M_a D_{bin}\nabla x_v \tag{46}$$

The net fluxes of liquid water, gas and water vapor with respect to the ground frame are computed from Eqs. (42), (43) and (46), respectively, as

$$\overline{n}_{w,G}=\rho_w\overline{v}_{w,s}-D_{w,cap}\nabla c_w+c_w\overline{v}_s \tag{47}$$

$$\overline{n}_{g,G}=\rho_g\overline{v}_{g,s}+c_g\overline{v_s} \tag{48}$$

$$\overline{n}_{v,G}=\rho_v\overline{v}_{g,s}-\left(\frac{C_g^2}{\rho_g}\right)M_v M_a D_{bin}\nabla x_v+c_v\overline{v}_s \tag{49}$$

2.3.4. Energy balance

One energy balance equation is solved for the mixture assuming thermal equilibrium between the different phases. Conservation of energy includes convection due to bulk flow of the phases, heat conduction and evaporation/condensation:

$$\rho_{eff}C_{p,eff}\frac{\partial T}{\partial t}+\sum_{i=w,v,a}(\overline{n}_{i,G}\nabla(C_{p,i}T))=\nabla(k_{eff}\nabla T)-\lambda\dot{I} \tag{50}$$

where $\dot{I}$ is the volumetric rate of evaporation. The properties of the mixture, $\rho_{eff}, C_{p,eff}, k_{eff}$, are obtained by averaging those of pure components, weighted by either their mass or volume fractions:

$$\rho_{eff}=(1-\phi)\rho_s+\phi(S_w\rho_w+S_g\rho_g) \tag{51}$$

$$C_{p,eff}=m_s C_{p,s}+m_w(S_w C_{p,w}+m_g C_{p,g}) \tag{52}$$

$$k_{eff}=(1-\phi)k_s+\phi(S_w k_w+S_g(\omega_v k_v+\omega_a k_a)) \tag{53}$$

2.3.5. Phase change

Evaporation of liquid water to vapor results in the development of large internal pressures within the kernel and, based on this, evaporation/condensation is modeled as being spatially distributed throughout the domain. An explicit expression for the evaporation rate, $\dot{I}$, is used in which the evaporation rate is proportional to the difference between actual vapor density and density of vapor at equilibrium (also known as saturation vapor density) and is given by

$$\dot{I}=K_{evap}(\rho_{v,eq}-\rho_v)S_g\phi \tag{54}$$

where $\rho_v=\rho_g\omega_v$ is the vapor density at any location inside the material (obtained as a model output from c_v), $\rho_{v,eq}$ is the saturation vapor density (obtained from moisture sorption isotherm of the material) and K_{evap} is the evaporation rate constant. Values of the evaporation rate constant are chosen by increasing it until the solution is independent of K_{evap} (Halder et al., 2007).

2.4. Boundary and initial conditions

Boundary conditions for the governing equations are now described and are also shown in Fig. 4. Initial conditions are listed with the input parameters (Table 1).

2.4.1. Solid mechanics

Displacements normal to the axisymmetric (boundary 1) and symmetry planes (boundary 3) are set to zero while the other boundary (boundary 2) is unconstrained and free to deform.

2.4.2. Multiphase transport

The rice kernel puffs at ambient pressures and, therefore, pressure equal to atmospheric pressure is used for Eq. (33):

$$p|_{surf}=p_{amb} \tag{55}$$

Liquid water moves from the interior to the surface (Eq. (32)) and leaves as vapor through surface evaporation, leading to the convective boundary condition:

$$\overline{n}_{w,s}|_{surf}=h_m\phi S_w(\rho_v-\rho_{v,amb}) \tag{56}$$

Note above that the flux of moisture at the surface is defined with respect to the deforming solid. In addition to water lost through

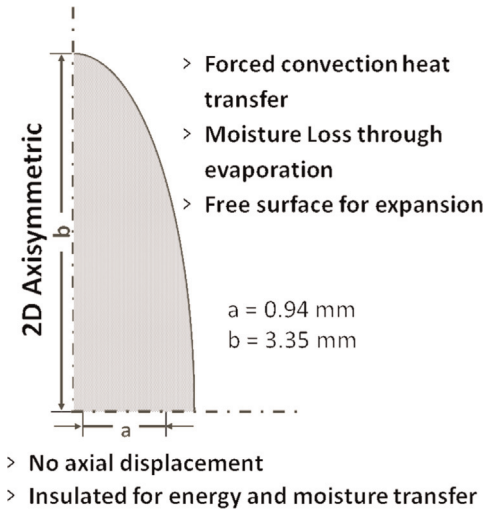

Fig. 4. Schematic showing the rice geometry used for simulations and boundary conditions for coupled solid mechanics – multiphase transport model.

evaporation, the moisture flux at the boundary also moves along with the movement of the surface due to expansion. Therefore, the total moisture lost from the surface with respect to the ground frame is given by

$$\overline{n}_{w,G}|_{surf} = \overline{n}_{w,s}|_{surf} + c_w \overline{v}_s \tag{57}$$

Water vapor reaches the surface (Eq. (34)) and is convected away. As above, the vapor flux at the boundary will have to be updated to account for the deforming surface:

$$\overline{n}_{v,s}|_{surf} = h_m \phi S_g (\rho_v - \rho_{v,amb}) \tag{58}$$

$$\overline{n}_{v,G}|_{surf} = \overline{n}_{v,s}|_{surf} + c_v \overline{v}_s \tag{59}$$

For energy equation (Eq. (50)), forced convective heat transfer takes place at the boundary:

$$q|_{sur} = h_t (T_{salt} - T_{surf}) - \lambda \overline{n}_{w,s}|_{surf} - \sum_{i=w,a} (\overline{n}_{i,G}|_{surf}) C_{p,v} T_{surf} \cdot \overline{N}_{surf} \tag{60}$$

In Eq. (60), the first term on the RHS is the convective heat transferred from the heating medium to the kernel surface, the second term is the heat lost due to surface evaporation of liquid water and the third term is the energy lost due to bulk flow gas normal to the surface ($\overline{N}_{surf}$ is the unit surface normal).

2.5. Input parameters

Input parameters used for simulating the rice puffing process are summarized in Table 3.1. Details about some of the important parameters are discussed here.

2.5.1. Glass transition temperature

Glass transition temperature, T_g, marks the onset of glassy–rubbery phase transition of materials that takes place over a small range of temperature. The T_g value of gelatinized (amorphous) rice starch for the range of moisture content considered in the present study is about 95 °C (Chung et al., 2002). During puffing, when the temperatures rise beyond the T_g value, there is a sharp change in the mechanical properties (see section below). Chung et al. (2002) report that the T_g value of native (un-gelatinized) crystalline rice starch is at least 20 °C higher when compared with the gelatinized counterpart. It is probably due to this reason that raw rice consisting of native crystalline starch does not puff as much since the onset of glassy–rubbery transition takes place at a higher temperature compared with parboiled rice (consisting of amorphous starch) when subjected to similar puffing conditions.

2.5.2. Mechanical properties

Mechanical properties, e.g., elastic modulus (E) and Poisson's ratio (ν) of rice, are needed as functions of glass transition temperature, T_g. Rice starch is initially glassy and when heated to high temperatures, it undergoes a phase transformation to rubbery state. Consequently, the magnitude of elastic modulus decreases drastically as the temperature increases through the T_g value. For rice starch in its glassy state, E_g and ν_g have been measured experimentally as 500 MPa and 0.28, respectively (Shitanda et al., 2002). In the rubbery state, elastic modulus of starch, E_r, has been estimated to be of the order of 1 kPa (Schwartzberg et al., 1995; Alavi et al., 2003a,b; Wang et al., 2005; Fan et al., 2012). This shows a reduction of several orders of magnitude in the elastic modulus across glass transition that allows for the large expansion of the rice kernel during puffing. For a soft and compliant material, Poisson's ratio in rubbery state, ν_r, is expected to be about 0.5; a value of 0.49 was used during computations to avoid singularity and help with convergence of the numerical scheme. It is worthwhile to mention here that starch behaves in a manner similar to other amorphous thermoplastic polymers, e.g., polycarbonate and polymethyl methacrylate when heated spanning their glass transition temperature (Richeton et al., 2007; Srivastava et al., 2010).

The temperature dependency of elastic modulus and Poisson's ratio, taking into account the glass transition temperature, T_g, were approximated by the following functions (Dupaix and Boyce, 2007):

$$E(T) = \frac{1}{2}(E_g + E_r) - \frac{1}{2}(E_g - E_r) \tanh\left(\frac{T - T_g}{\beta}\right) \tag{61}$$

$$\nu(T) = \frac{1}{2}(\nu_g + \nu_r) - \frac{1}{2}(\nu_g - \nu_r) \tanh\left(\frac{T - T_g}{\beta}\right) \tag{62}$$

Here, β is a parameter related to the temperature range across which glass transition occurs. A value of $\beta = 5$ °C was assumed based on values reported for other glassy polymers (Srivastava et al., 2010). Fig. 5 shows the changes in mechanical properties across the glass transition temperature used in this study based on discussions in this section. One can clearly observe a sharp change in property values as the material transitions to the rubbery state.

Now, for the constitutive equation (Eq. (20)), shear modulus, G, and bulk modulus, K, are needed. These are obtained in terms of E and ν through standard equations available from solid mechanics literature:

$$G(T) = \frac{E(T)}{2(1 + \nu(T))} \tag{63}$$

$$K(T) = G(T) \frac{2(1 + \nu(T))}{3(1 - 2\nu(T))} \tag{64}$$

The yield stress of starch is obtained as a function of temperature (Alavi et al., 2003a,b) and is listed in Table 1.

2.5.3. Porosity factor

During puffing, the rice kernel undergoes large volume expansion resulting in significant changes in the porosity of the material as can be seen in Eq. (5). As the porosity of the material increases, it becomes more permeable to the flow of fluid phases. This is accounted for by changing the liquid and gas permeabilities by multiplying a porosity factor given by Kozney–Carman equation (Bear, 1972):

$$f(\phi) = \left(\frac{\phi}{\phi_0}\right)^3 \left(\frac{1 - \phi_0}{1 - \phi}\right)^2 \tag{65}$$

Table 1
Input parameters used in the simulations for rice puffing.

Parameter	Value	Units	Source
Dimensions			
Major axis, a	3.363	mm	This study
Major axis, b	0.944	mm	This study
Density			
Water, ρ_w	998	kg/m^3	McCabe et al. (2005)
Vapor, ρ_v	Ideal gas	kg/m^3	
Air, ρ_a	Ideal gas	kg/m^3	
Solid, ρ_s	1564	kg/m^3	Fukuoka et al. (2000)
Specific heat capacity			
Water, c_{pw}	$4176.2-0.0909(T-273)+5.4731\times10^{-3}(T-273)^2$	J/kg K	Lewis (1987)
Vapor, c_{pv}	$1790+0.107(T-273)+5.856\times10^{-4}(T-273)^2-1.997\times10^{-7}(T-273)^3$	J/kg K	Lewis (1987)
Air, c_{pa}	1006	J/kg K	Choi and Okos (1986)
Solid, c_{ps}	1800	J/kg K	Choi and Okos (1986)
Thermal conductivity			
Water, k_w	$0.57109+0.0017625T-6.7306\times10^{-6}T^2$	W/m K	Choi and Okos (1986)
Vapor, k_v	0.026	W/m K	Choi and Okos (1986)
Air, k_a	0.026	W/m K	Choi and Okos (1986)
Solid, k_s	0.21	W/m K	Choi and Okos (1986)
Intrinsic permeability			
Water, $k_{in,w}$	1×10^{-20}	m^2	Warning et al. (2014)
Air and vapor, $k_{in,g}$	$k_{in,w}\left(1+\frac{0.15k_{in,w}^{-0.37}}{p}\right)$	m^2	Tanikawa and Shimamoto (2009)
Relative permeability			
Water, $k_{r,w}$	$f(\phi)\times((S_w-0.09)/0.91)^3,\ S_w>0.09$ $0,\ S_w<0.09$		Bear (1972)
Air and vapor, $k_{r,g}$	$f(\phi)\times(1-1.1S_w),\ S_w<0.91$ $0,\ S_w>0.91$		Bear (1972)
Capillary diffusivity			
Water, $D_{w,cap}$	$1.35\times10^{-8}\times\exp\left[\frac{-21.61(548-T)(1.194+3.68M)}{T(1+18.98M)}\right]$	m^2/s	van der Lijn (1976)
Viscosity			
Water, μ_w	0.988×10^{-3}	Pa s	McCabe et al. (2005)
Air and vapor, μ_g	1.8×10^{-5}	Pa s	McCabe et al. (2005)
Heat transfer coefficient, h_t	100	W/m^2 K	Das (2005)
Mass transfer coefficient, h_m	0.15	m/s	Murthy et al. (2009)
Latent heat of vaporization, λ_{vap}	2260×10^5	J/kg	Schwartzberg et al. (1995)
Vapor diffusivity in air, $D_{eff,g}$	$\frac{2.13}{p}\left(\frac{T}{273}\right)^{1.8}(S_g\phi)^{3-\phi}/\phi$	m^2/s	Moldrup et al. (2005)
Saturation vapor pressure, p_{sat}	$1002.2\times\exp\left(9.437-\frac{3867.44}{T-43.37}\right)$	kPa	
Equilibrium vapor pressure, $p_{v,eq}$	$p_{sat}\times\left(B\times M+\frac{C\times M}{F+M}\right)$	kPa	Wu and Schwartzberg (1994)
	$B=-0.5362-0.001394T+\frac{2.0474(468.9-T))}{477.42-T)}$	–	
	$C=-0.2479+0.001216T$	–	
	$F=-0.002004+0.3165\times10^{-5}T$	–	
Ambient pressure, P_{amb}	101,325	Pa	
Ambient temperature, T_{amb}	200	°C	
Young's modulus, E	Eq. (61)	Pa	Srivastava et al. (2010)
Shear modulus, G	Eq. (63)	Pa	
Bulk modulus, K	Eq. (64)	Pa	
Yield stress, σ_0	$2000\times\exp(0.013(300-T))$	Pa	Alavi et al. (2003a,b)
Initial conditions			
Porosity, ϕ_0	0.1840	–	
Pressure, P_0	101,325	Pa	
Water concentration, $c_{w,0}$	164	kg/m^3	
Vapor mass fraction, ω_0	1.884×10^{-4}	–	
Temperature, T_0	22	°C	

3. Solution methodology geometry, mesh and implementation

An actual 3D geometry for the rice kernel could not be used for the present study due to the massive computing resources that would be needed. Instead, the kernel was assumed to be a prolate spheroid and, owing to symmetry, 2D axisymmetric geometry was used for this study. The average dimension of ten rice grains (described in Section 4) was used to create a quarter ellipse, as shown in Fig. 4. A triangular mesh consisting of 10,800 elements was used with more elements along the boundary of the kernel to help with convergence (Fig. 6).

A commercially available finite element software COMSOL Multiphysics 4.3b (Comsol Inc., Burlington, MA) was used to solve the governing equations described in Section 2.3. Solid momentum balance (Eq. (14)) was solved in the Lagrangian frame of reference using the Structural Mechanics module. Mass conservation equations for liquid water, gas and water vapor (Eqs. (32)–(33)) were solved in the Eulerian frame (frame with respect

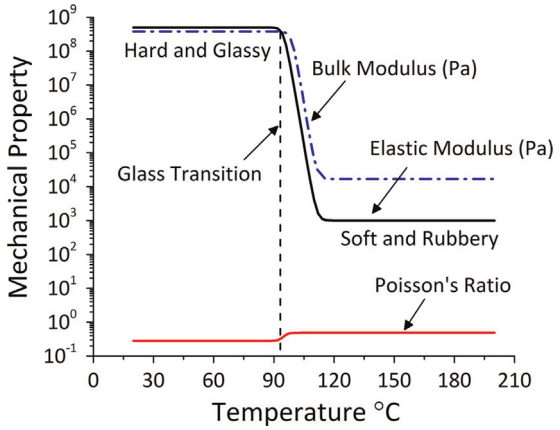

Fig. 5. Mechanical property changes with temperature. Note the sharp change in properties across the glass transition temperature.

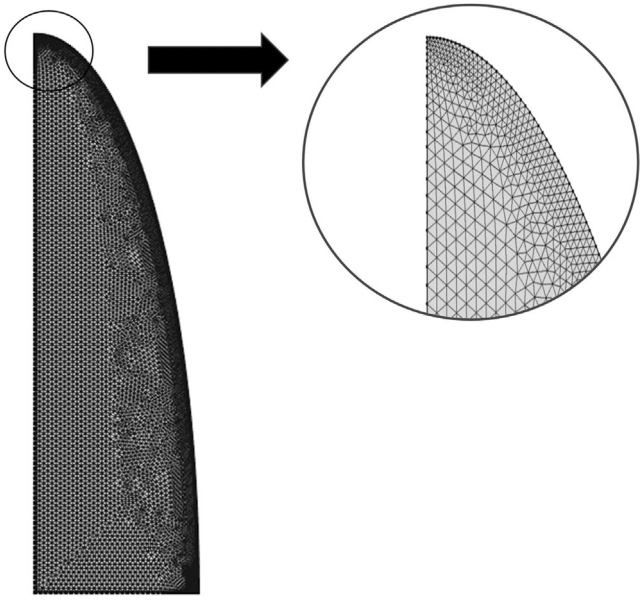

Fig. 6. Meshed geometry with triangular mesh elements. Mesh density is higher near the tip of the kernel and at the boundary (see expanded view) to help convergence.

to a stationary observer) using Transport of Dilute Species, Darcy's Law and Transport of Concentrated Species modules, respectively. For all the variables, linear shape functions were used. Due to complex coupling of governing equations together with non-linear material properties, the direct solver PARDISO was used. Variable time stepping with a maximum time step size of 0.001 s was used to solve the problem. The simulation of 15 s of puffing took approximately 64 h of CPU time on a 2.0 GHz 12-core Intel Xeon Workstation with 32 GB RAM.

4. Experimental methodology

4.1. Puffing experiments

Rice puffing experiments were carried out using a long grain parboiled rice variety (Goya Golden Canillar Parboiled Rice, Secaucus, NJ) procured from a local supermarket. The initial moisture content of rice was measured gravimetrically and was found to be 12% (wet basis). Puffing was conducted by toasting rice in a hand held iron pan consisting of 300 g of fine salt (Morton white fine plain table salt, Chicago, IL) heated using an induction cooktop (Duxktop 1800-Watt Portable Induction cooktop) having a temperature control setting. A portable digital thermometer with K-type thermocouple probe (Omega Engineering Inc., Stamford, Connecticut, USA) was used to measure the temperature of the salt bed to ensure that the temperatures reached 200 ± 5 °C before the rice was put in the pan. Rice (about 20 g for one set of experiments) was puffed for different puffing times of 3, 6, 9, 12, 15 s. Several sets of experiments were conducted for each puffing time. For every set, 15 g of salt for every 1 g of rice was used to ensure optimum heat transfer between the salt bed and the rice kernels (Chinnaswamy and Bhattacharya, 1983). After each experiment, the rice samples were separated from salt using a strainer that allowed only the salt to pass through. This was done quickly enough ($\sim$1 s) to ensure that the samples were representative of that puffing time. Finally, the samples were stored in zip-lock bags at 22–25 °C to prevent moisture uptake.

4.2. Measurement of volume expansion ratio, dimension changes and moisture content

For rice samples puffed at different times, volume expansions were measured following published protocols (Chinnaswamy and Bhattacharya, 1983; Hoke et al., 2007). Fifty grains of rice were placed inside 10 and 20 ml measuring cylinders and the remaining space was filled with fine salt. The cylinders were tapped several times to ensure that the salt filled up the pores between the grains. The total volume of 50 grains was obtained by subtracting the volume occupied by the salt from the total volume of the cylinder. Three replicates were carried out for each measuring cylinder. The expansion ratio of the kernels puffed at different times was obtained by dividing the volume expansion at any instant with the volume of un-puffed grains (i.e., at $t=0$ s). The length and diameter of grains puffed for different times were measured using a vernier caliper. Dimensions of 10 grains were measured for each set. Moisture measurements of grains (2 g) for different puffing times were carried out using the AOAC protocol. Three replicates were carried for each measurement.

4.3. Obtaining micro-CT scan and porosity profiles

Rice kernels at different puffing times were scanned at Cornell University's MicroCT imaging facility. Scans were made using ZEISS/Xradia Versa 520 X-ray Microscope (CT) (Carl Zeiss, Jena, Germany). The scan obtained 1040 projections at 0.35° intervals over 360° using 80 keV, 32 mA, 100 ms exposure time and 10 μm x–y–z voxels. The 2D slices obtained from the CT scan were reconstructed in Avizo Fire™ (FEI Visualization Sciences Group, Hillsboro, Oregon) using appropriate filtering algorithms to construct a 3D volumetric dataset. This was followed by image segmentation using the watershed separation technique that is routinely used for such purposes (Bostwick et al., 2012). This enabled (1) isolation of the pores from the material; (2) visualization of the internal microstructure and spatial porosity profiles of the rice at different puff times, and (3) calculation of gas porosity in the puffed rice for different puff times.

5. Results and discussion

The model developed was validated by comparing moisture loss, expansion ratio and dimension change histories of the puffed rice. Transient changes in temperature, liquid water saturation, pressure, evaporation, porosity development and stresses and strains that generate inside the kernel are discussed next. This is followed by sensitivity analysis and process optimization with

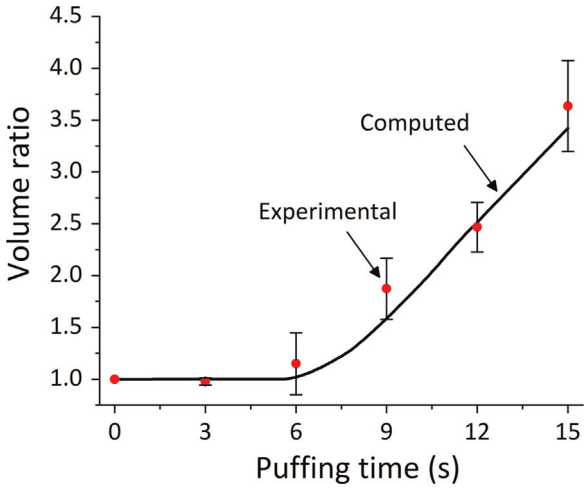

Fig. 7. Computed and measured volume expansion ratio of the rice kernels as a function of puffing time.

respect to key parameters that affect the final volume and moisture content of puffed rice and model extension to the process of gun-puffing.

5.1. Experimental validation: expansion ratio, dimensions and moisture loss histories

Expansion ratio (i.e., ratio of final to initial volume) history of rice puffed for different times is shown in Fig. 7 along with model predictions. The trend of volume expansion predicted by the model follows the experimentally observed values closely, although the model slightly under predicts the expansion ratio towards the end. This is probably due to higher values of permeability and bulk modulus of the material used for computation. Intrinsic permeability and bulk modulus of the solid are two important factors that affect volumetric expansion (Rakesh and Datta, 2012). Lower values of both intrinsic permeability and bulk modulus favor large volume of the puffed product since a lower permeability would result in more pressure build-up within the kernel and a low bulk modulus would allow for a larger expansion. Accurate values of permeability and bulk modulus are difficult to obtain due to several experimental difficulties (Schwartzberg et al., 1995; Halder et al., 2011). Therefore, sensitivity analysis is carried out later (Section 5.7) with respect to these two parameters to study their effects on the expansion of the puffed rice. Moreover, a large variation in the experimental values of volume ratio, especially during the later portions of the puffing process, is seen. This could be due to several factors some of which are: (1) the presence of ungelatinized starch in the parboiled rice that can potentially consume water and undergo starch gelatinization leading to less water available for vapor generation (van der Sman and Broeze, 2013), (2) variation in the initial moisture content between individual grains – a low initial moisture content value would result in a lower final expansion, and (3) a higher degree of contact with salt (heating medium) leading to a quick temperature rise and an early glassy–rubbery phase transition leading to more expansion (see Section 5.2 for further details). These factors could possibly explain the variability observed in experimental results.

From Fig. 7, it is observed that the volumetric expansion is almost negligible for the initial few seconds (~6 s). This is due to low pressures inside the kernel and a large bulk modulus since rice is in its glassy state. During the initial period, the temperatures are not sufficiently high to generate high pressures and mechanical properties, being a function of glass transition temperature, are high enough to resist volume changes of the kernel. As the material heats further and undergoes the glassy to rubbery phase transition, it starts to become more soft and compliant (see Fig. 5 for details). *The glassy–rubbery transition begins from the tip where the temperatures are higher and then proceeds to the sides and finally to the core causing the entire kernel to puff.* Fig. 8 compares experimentally observed changes in length and diameter of rice with those predicted by the model and shows good agreement.

Fig. 9 shows good agreement between predicted and experimentally measured moisture content of the rice kernel at different times during the puffing process. During the initial few seconds, moisture loss takes place primarily via surface evaporation. Later, much of the liquid water is lost due to internal evaporation as the material expands, resulting in a rapid decrease in liquid water soon after 6 s, that also starts the puffing process. Due to expansion, gas pressure within the kernel reduces significantly. Consequently, there is a sharp decrease in the saturation temperature of liquid water given by saturation pressure versus temperature curve. Liquid water that was initially superheated undergoes phase change to water vapor when the pressure is suddenly released due to volume expansion. The slight discrepancy between model predictions and experimental values is probably due to more internal evaporation predicted by the model. Nevertheless, the predicted moisture history is in good agreement with that experimentally observed.

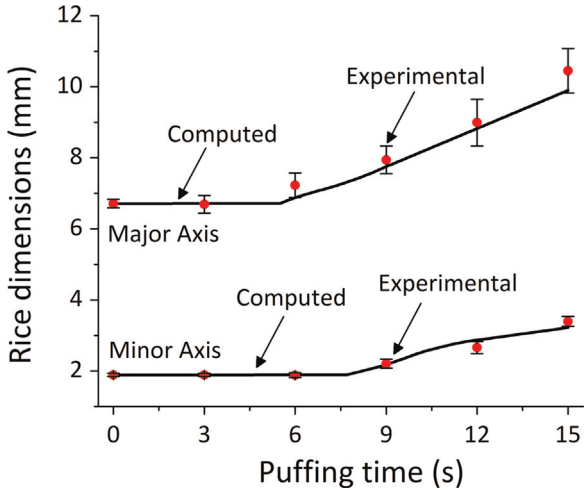

Fig. 8. Computed and measured changes in dimensions (major and minor axis) of the rice kernels at different puff times.

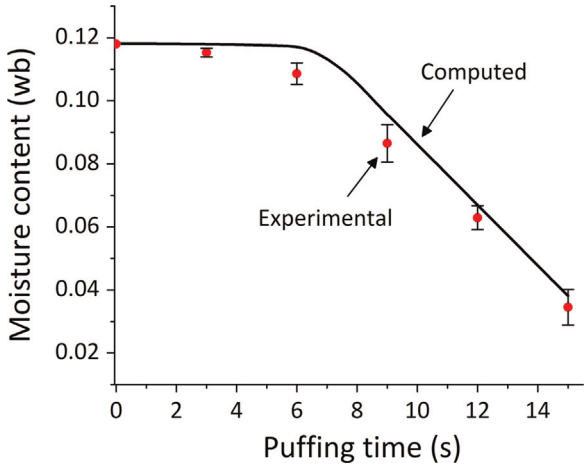

Fig. 9. Changes in predicted and experimentally observed moisture content (wet basis) of the rice kernels at different puff times.

As is expected, there is definitely a significant variation in property values of individual rice kernels that may not lead to an accurate prediction. Moreover, rice puffing is a very quick process with large changes occurring in the material that affect transport and solid mechanical properties in a significant way leading to some discrepancy between experiment and model predictions. However, based on experimental measurements of volume expansion, dimension changes and moisture content histories, the trends predicted by the model closely follow those observed experimentally, and the puffing model developed is therefore considered validated. The next sections present additional results followed by sensitivity analysis and optimization.

5.2. Temperature distribution

Computed temperature profiles at different instants of puffing are shown in Fig. 10. The temperatures begin to rise from near the tip of the kernel (multidimensional heating) resulting in an increased rate of evaporation. This results in an increase in gas pressure locally creating the necessary gradient for the material to puff near those locations. However, due to large internal evaporation, there is more evaporative cooling and the temperatures do not rise as much within the kernel. This prolongs the glassy–rubbery phase transition of the material. As a consequence, material expansion is not significant up until about 6 s. As the temperature increases further and crosses the glass transition temperature (near the tip), there is a significant reduction in the mechanical properties of the material, especially the bulk modulus. Since the necessary pressure gradient already exists, the material begins to puff around those locations. Fig. 11 shows the changes in the bulk modulus of the material at different instants of puffing. Expansion of the grain starting near the tip is verified experimentally in Fig. 12 that shows the shapes of the rice kernels at different times during puffing. The starch undergoes expansion near the tip (at about 6 s) where the temperatures have crossed the T_g value. At this stage, the sides of the kernel remain hard and glassy. With time, heat flows into the material from the sides and temperatures begin to rise at those regions eventually leading to glass transition at the sides followed by the entire kernel phase transforming into the rubbery state from within the core. This begins to happen at around 9 s at which time, the material starts to expand from the sides (Fig. 12) and at about 15 s, the entire kernel is puffed. Note, the kernel temperature does not reach puffing temperatures because of a progressive development of the gas phase within and evaporative cooling due to phase change. Due to increase in concentration of the gas phase, the effective thermal conductivity (Fig. 13) of the material decreases with time that prevents the internal temperatures to rise to puffing temperatures.

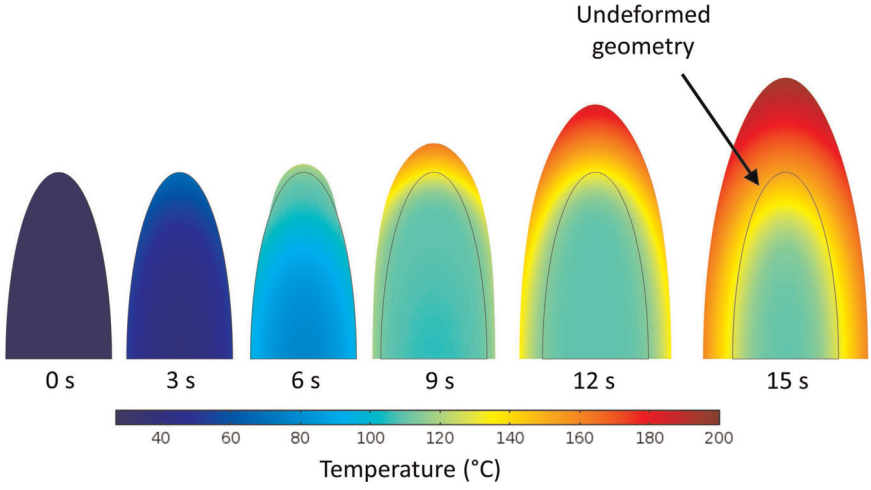

Fig. 10. Computed temperature profiles inside the rice kernel at different puff times.

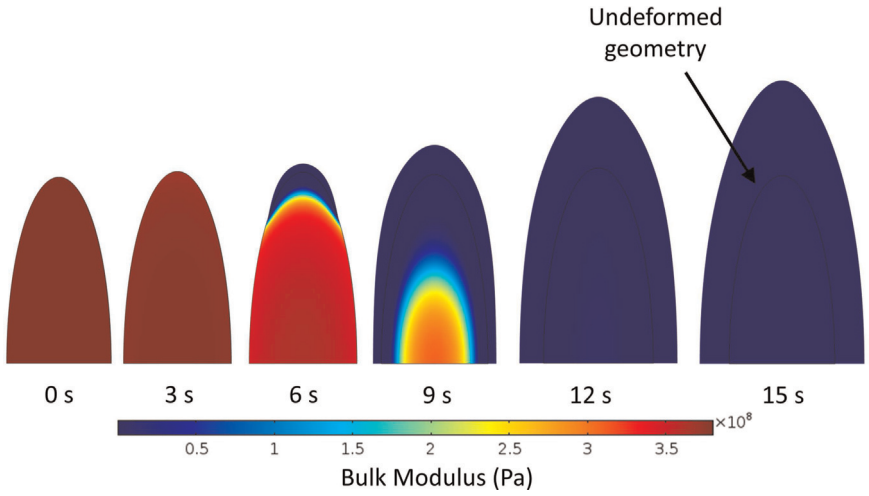

Fig. 11. Changes in bulk modulus of the rice kernel at different puff times. Note the sharp decrease in the bulk modulus values due to glass transition.

5.3. Liquid water saturation

Fig. 14 shows the spatial variation of relative saturation of liquid water, S_w, inside the rice kernel at different times during the puffing process. Initially, the pores are almost saturated with water with very little gas phase. As the temperature of the kernel starts to rise, the rate of evaporation increases resulting in a build-up of pressure inside the hard glassy kernel. Since the pressures are high, liquid water would boil at a higher temperature. With further increase in temperature, as noted above, the material transitions into the rubbery state allowing the matrix to expand. As a result of volume expansion, pressures reduce drastically causing the liquid water to phase change to water vapor. A sharp change in the S_w value is observed in the puffed and unpuffed regions of the kernel with S_w values approaching zero in the expanded regions. Thus, the two regions are equivalent to dried and wet regions. A direct consequence of decrease in liquid water saturation is an increase in the saturation of gas phase resulting in an increase in gas porosity (discussed in detail in Section 5.5).

5.3.1. Relative magnitudes of liquid water flux

The liquid water inside rice experiences both convective and diffusive flux when heated. Fig. 15 shows the magnitudes of diffusive flux (due to capillarity) and convective flux (due to pressure driven flow) with time during the puffing process. Initially, the convective flux is the dominant mode of transport due to large pressure generation inside the material. However, when the material starts to puff, pressures reduce significantly, decreasing the magnitude of convective flux (see Section 5.4 for discussion on pressure). The diffusive flux increases gradually and picks up at about 6 s, at which time, the gradients in liquid water concentration, c_w, increase significantly. The profiles for liquid water

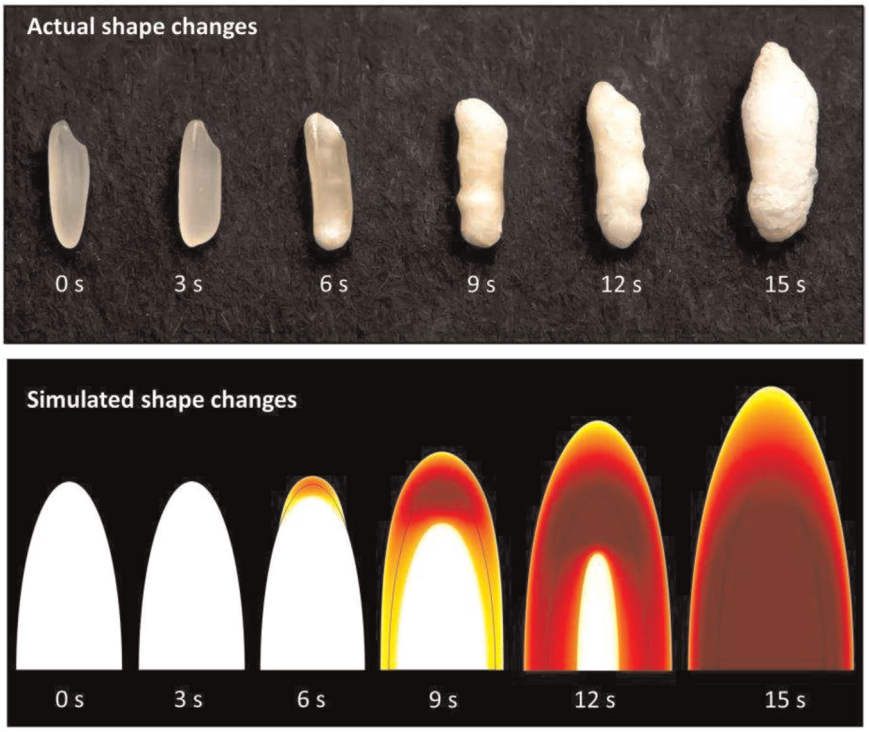

Fig. 12. Computed and experimentally observed shape changes of the rice kernel at different puff times. Puffing begins from the tip of the kernel as seen in experiments and computed shape changes. The times for experimental images are within ± 1 s of those indicated.

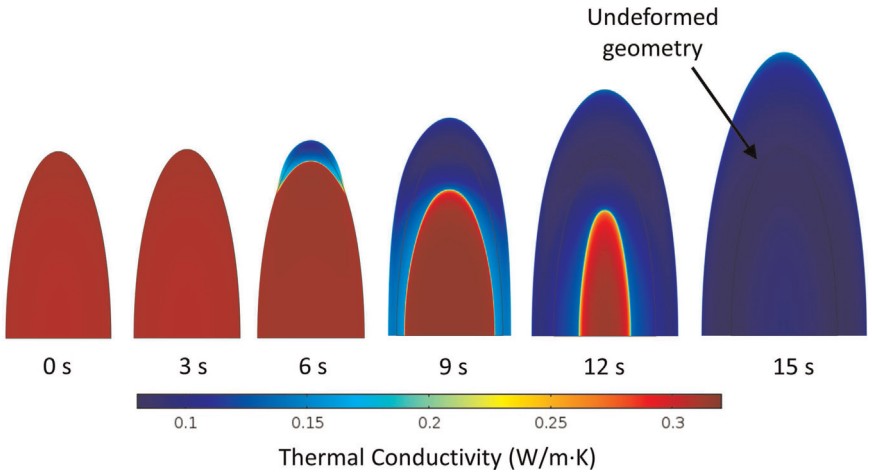

Fig. 13. Variation of effective thermal conductivity of the rice kernel at different puff times. The k_{eff} value reduces drastically as more gas phase develops during puffing.

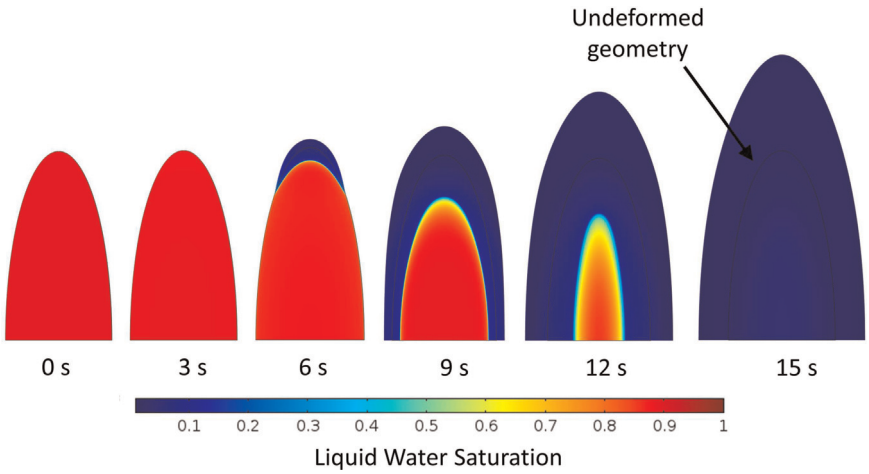

Fig. 14. Computed liquid water saturation, S_w, of the rice kernel at different puff times. The S_w value reduces significantly due to "flash-off" of water when the material expands.

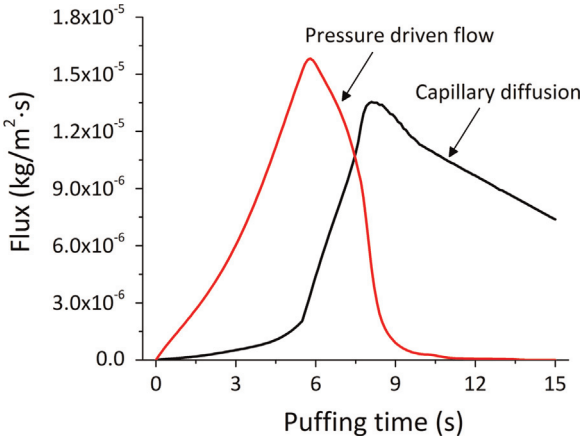

Fig. 15. Magnitudes of pressure driven flow and capillary diffusion during rice puffing. It is observed that both modes are equally important to consider for puffing-type processes.

concentration follow similar trends with S_w (Fig. 14) showing the large gradient between the core and the regions near the surface. With time, gradients in c_w reduce, decreasing the diffusive flux towards the later portions of the puffing process. Fig. 15 indicates that both pressure driven flow and capillary diffusion are equally important for puffing processes and both transport mechanisms need to be included in the modeling framework for better predictions of process parameters.

5.4. Rate of evaporation and pressure development

Figs. 16 and 17 show the computed evaporation rate and pressure development within the kernel at different times during puffing. Evaporation begins from the tip where the temperatures are high and progresses towards the interior. Almost a sharp evaporation front is observed at the glassy–rubbery interface inside the rice kernel. Initially, the evaporation rate is high due to a large temperature gradient at the surface leading to a high rate of heat transfer. As the material puffs, the rate of evaporation reduces due to a decrease in temperature difference and reduced rate of heat transfer. Since the puffed portion of the kernel is composed primarily of air, the effective thermal conductivity is small (see Fig. 13) thereby reducing the rate of heat transfer to the core and thus contributing to lower evaporation rates.

The regions of high pressure (Fig. 17) correspond with regions of lower permeability (Fig. 18). Due to lower permeability of the material (i.e., when the material is unpuffed) and internal evaporation, the developed gas pressure is significant (see Fig. 17 at 3 and 6 s). The calculated peak pressure (1.6 MPa) is higher than what was measured for corn puffing (~1.0 MPa Schwartzberg et al., 1995) probably due to lower intrinsic permeability of rice and higher rates of evaporation as computed by the model. When the material undergoes glass transition, it becomes soft and allows for the large volume expansion of the material locally due to large pressure gradients that exist. When the material expands, the pressures are released in the expanded regions. This begins to happen from near the tip as was discussed earlier. As the material transitions at the sides and finally in the core, expansion occurs all throughout the material and pressures are released with values eventually reaching atmospheric pressures in the expanded product. The peak pressure is reached just before puffing begins since the evaporation rate is high and permeability of the material is low. Peak pressures reduce with time due to: (1) decreasing rates of evaporation due to reasons noted above and (2) increasing permeability of the material through the Kozney–Carman porosity factor (Fig. 18). An increase in permeability with time results in less resistance to flow of gases contributing toward lower values of pressure.

5.5. Microstructure and porosity development

Fig. 19 shows the evolution of microstructure of the rice kernels constructed from micro-CT images and the gas porosity profiles as predicted by the model, respectively. The predicted porosity profiles are in good qualitative agreement with those observed experimentally. Pore formation starts from the tip where there is more expansion of the material (see, e.g., at 6 s in Fig. 19) and continues to the sides of the kernel (at about 9 s) and eventually the whole material becomes porous at 15 s.

Porosity is an important quality attribute associated with puffed products. A product that is more porous provides a crunchier mouthfeel. Porosity is measured routinely as opposed to being predicted. Mathematical models available for predicting porosity typically use fitting parameters derived from experimental measurements and are valid for a particular product-process combination only (Gulati and Datta, 2013). The modeling framework presented in this study allows us to predict porosity using fundamental conservation laws that require very little empirical information. The framework, therefore, is applicable to a large class of processes and products.

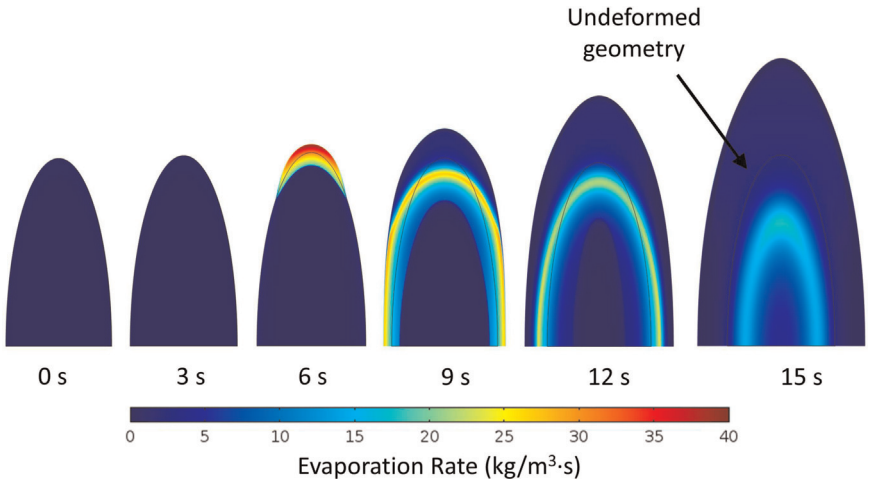

Fig. 16. Computed rate of evaporation, $\dot{I}$, inside the rice kernel at different puff times. Evaporation is spatially distributed within the domain resulting in gas pressure generation for puffing.

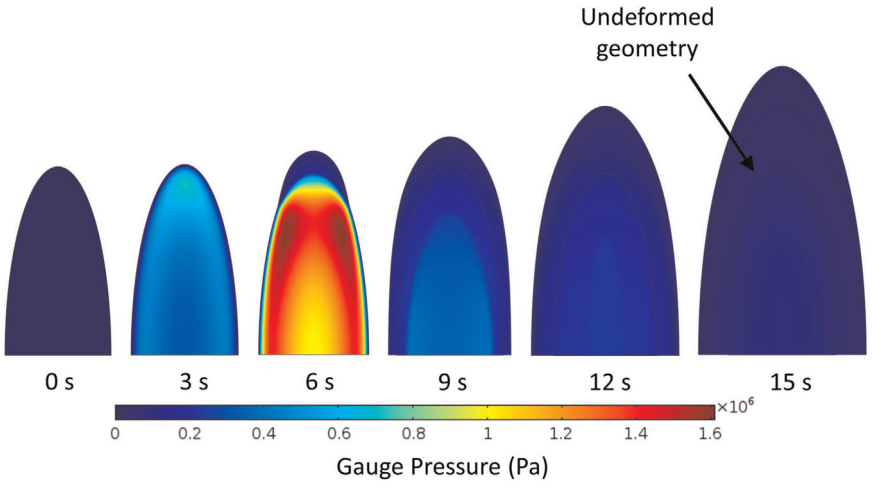

Fig. 17. Computed gas pressure, p_g, inside the rice kernel at different puff times. Gas pressure is highest near the glassy regions within the material.

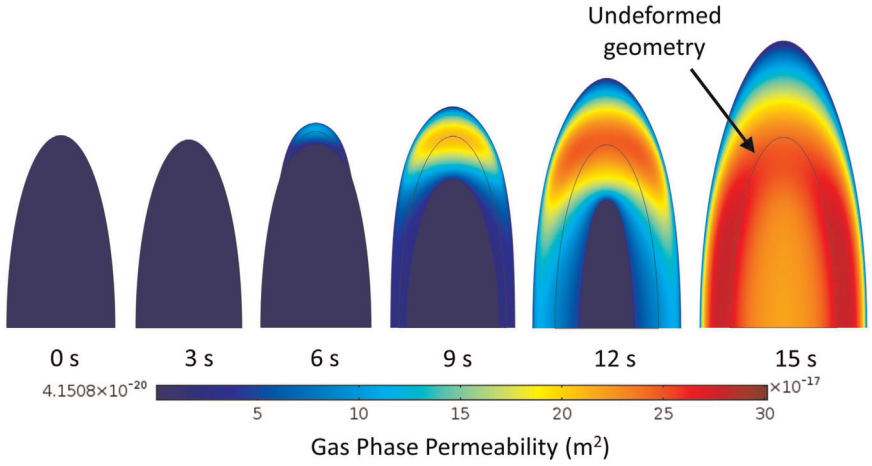

Fig. 18. Computed gas phase permeability, k_g, inside the rice kernel at different instants of puffing. There is a sharp increase in the permeability of the gas phase as the material expands due to Kozney–Carmen porosity factor.

In porous media literature, porosity is defined as the volume occupied by all the fluid phases and in a non-deforming material, the total porosity stays the same since liquid water changes to vapor and vice versa. The porosity can change only when the material undergoes some sort of deformation (shrinkage/swelling) such as during rice puffing. In food literature, porosity is defined as

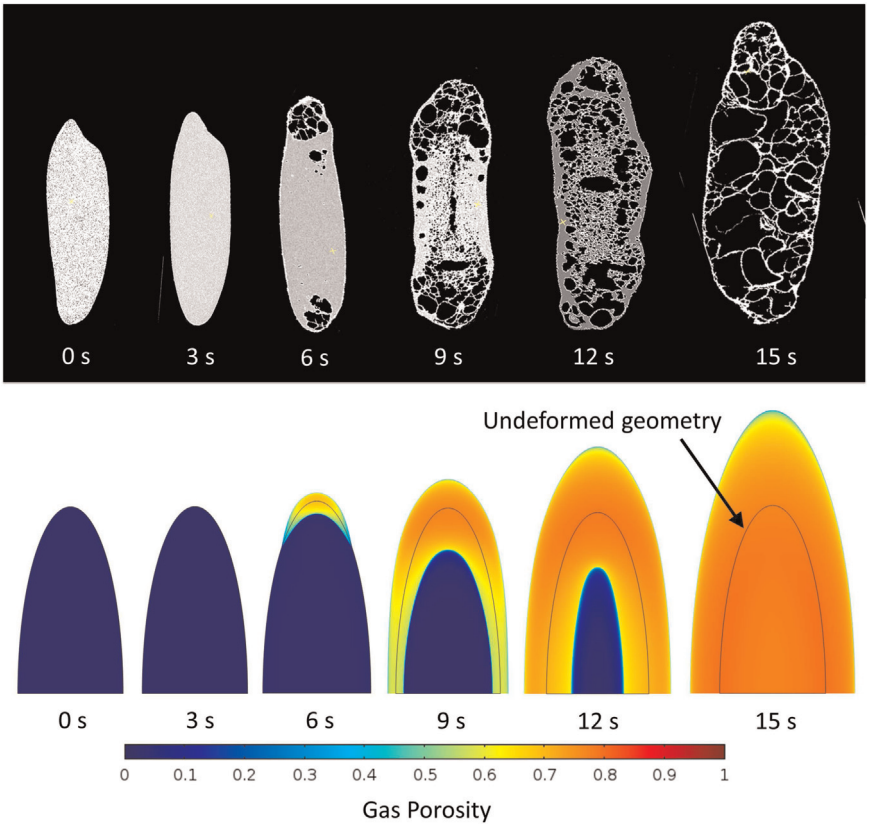

Fig. 19. Micro-CT scans of rise showing pore formation inside rice kernels along with predicted porosity profiles at different puff times.

the fraction of volume occupied by the gas phase to the total volume:

$$\phi_g = \frac{\Delta V_g}{\Delta V} = S_g \phi \tag{66}$$

Fig. 20 shows the changes in total porosity of the rice kernel and the evolution of gas porosity during puffing along with the porosity obtained from μ-CT scans of experimentally puffed rice kernels at different puffing times. Good agreement between the observed and computed gas porosity values serve as another key validation of the model. There is large variability in the experimental porosity values that can be attributed to the same reasons for variability in volume expansion of the material as noted in Section 5.1. In this figure, the total porosity increases due to volume expansion of the kernel whereas the gas porosity increases as liquid water evaporates to vapor as noted in Section 5.4.

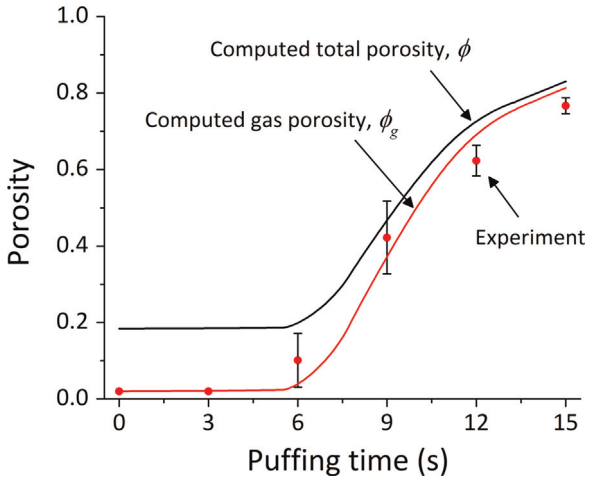

Fig. 20. Experimental and computed average gas porosity, ϕ_g, inside the rice kernel at different puff times.

5.6. Stress development during puffing

The gas pressure gradient is the driving force for stress development while the state of the material (rubbery or glass) determines its mechanical properties. Any shrinkage arising due to moisture loss is considered small and neglected. The state of the material manifests itself through mechanical properties – lower the bulk modulus, higher is the deformation. Fig. 21 shows the first principal tensile stress (i.e., the maximum stress level) inside the rice kernel at different instants of puffing. The regions of high stress correspond to the regions of glassy state and high pressure. Initially, stress builds up near the tip of the kernel (3 s) where the pressures are high (Fig. 17) and the material is glassy (Fig. 11). When puffing begins (6 s), the stress reduces near those locations since gradients in gas pressure subside locally and there is ease of expansion due to a drastic reduction in bulk modulus of the material as it reaches rubbery state. Generally, at any given instant of puffing, the stress levels are higher at the rubbery–glassy interface where the material has a tendency to expand more due to the presence of large pressure gradients but is unable due to higher mechanical properties. Finally, when the entire kernel is expanded (15 s), gradients in gas pressure become zero and the stresses subside. Fig. 22 shows the peak tensile stress and peak pressures that develop inside the material indicating that the stress development depends strongly on the gas pressure that builds up within the material.

5.6.1. Plastic deformations during puffing

Fig. 23 shows the elastic and effective plastic strain the solid experiences during puffing. Plastic deformation occurs when the

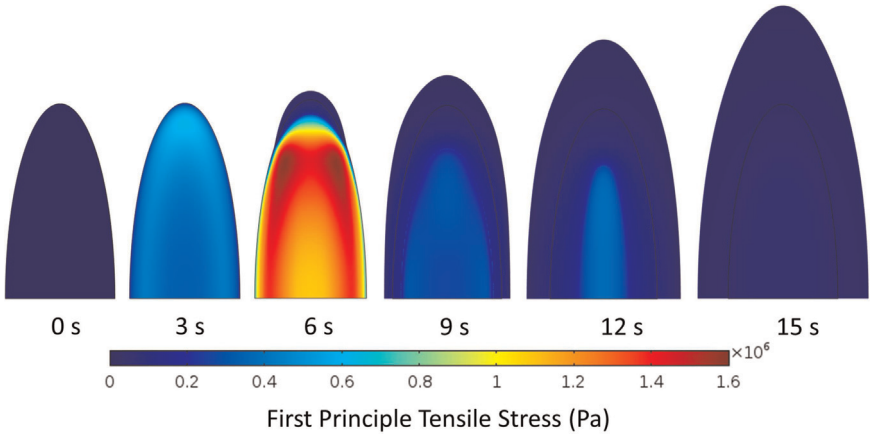

Fig. 21. Computed first principle tensile stress (max. stress) inside the rice kernel at different puff times. The regions of high stress corresponds with those of high gas pressures (Fig. 17).

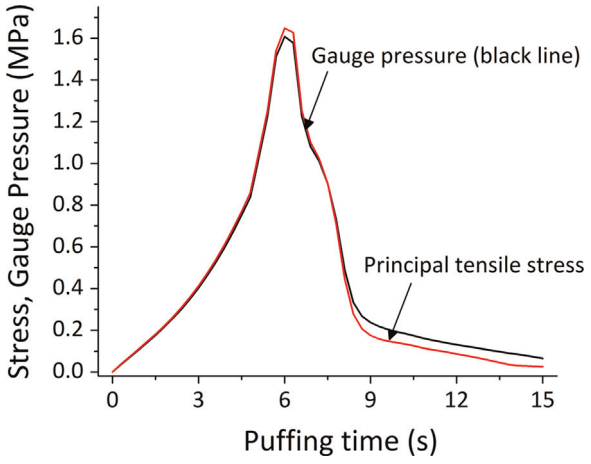

Fig. 22. Peak tensile stress and gauge pressure showing a one to one relationship between the two.

stress levels increase beyond the elastic limit at which point the material begins to yield (or flow). Fig. 23b shows large plastic strains (~400%) in the material that are much higher than the elastic strains (Fig. 23a). Since rice is composed primarily of starch, the large-chained starch molecules experience excessive elongation beyond their elastic threshold and even bond breakage leading to permanent deformations in the material. Fig. 24 shows the cross-sectional view of the rice microstructure at different instants of puffing. One can clearly observe the walls of the pores stretching as puffing proceeds resulting in the walls getting thinner with time. Additionally, at certain locations, it so happens that the walls become too thin and the stress due to gas pressure exceeds the failure stress of the material leading to pore rupture. This is similar to "necking" and failure of other thermoplastic polymers when stretched beyond the elastic limit and Considere's criterion can very well explain this phenomenon (Taki et al., 2006; Yue et al., 2007). Considere's criterion states that necking begins when the rate of strain hardening exceeds the stress in the material in the plastic regime. Once necking begins to happen, the stress becomes localized at a particular point on the solid skeleton. Further elongation occurs at reduced stress levels and this is followed by material rupture and pore coalescence. However, in this study, the material is assumed perfectly plastic without exhibiting any strain hardening and resulting in the stress being bounded by the yield stress.

It should be noted that the mechanics of starch expansion is quite complex and that starch also exhibits viscous properties at high temperatures. However, no data is available on extensional viscosity that would help understand and characterize the viscous deformation of starch at high temperatures (van der Sman and Broeze, 2013). Since starch exhibits both strain hardening and viscous effects, a viscoplastic constitutive model would be more appropriate. However, such models are quite complex requiring elaborate experimental setups and determining a large number of parameters and coefficients for the viscoplastic constitutive model which is beyond the scope of the present study.

5.7. Sensitivity analysis

A large number of input parameters are required for modeling the rice puffing process (Table 1). Given the unavailability of accurate values for some of them, it is important to perform a parametric sensitivity analysis in order to have greater confidence in the predicted results. For example, only estimated values of intrinsic liquid permeability of rice and bulk modulus of starch in the rubbery state are available. To determine how these affect the expansion of rice, sensitivity analysis was carried out for the two parameters. Bulk modulus and intrinsic permeability values were varied by $\pm 50\%$ and $\pm 1000\%$, respectively, and their effect on moisture content and volume expansion histories, two of the most important quality attributes associated with puffed products were computed.

5.7.1. Intrinsic permeability

Experimentally measured values of intrinsic liquid permeability of rice is not available in the literature. A permeability value of 10^{-20} m^2 was estimated for heat treated parboiled rice using Lattice Boltzman simulations (Warning et al., 2014) and was used for the reference case. The intrinsic permeability value was varied by $\pm 1000\%$ to include a large variation. Note here that both liquid and gas permeabilities affect volume expansion of the kernel. The liquid and gas permeabilities are related through the Klinkenberg effect (Tanikawa and Shimamoto, 2009) (see Table 1 for details) and, therefore, knowing the value of either of the two suffices. Fig. 25a shows the computed volume expansion ratio histories for the two values of intrinsic liquid permeability and is compared with the reference case. When the permeability is lower, there is more resistance to the flow of fluid phases through the porous media. As a consequence, pressures are higher inside the material resulting in more expansion. Fig. 25b compares the moisture loss histories for the different permeability values considered. The moisture content is slightly lower for a material having lower permeability because with higher expansion, subsequent pressure release is also higher. Consequently, there is a large decrease in the

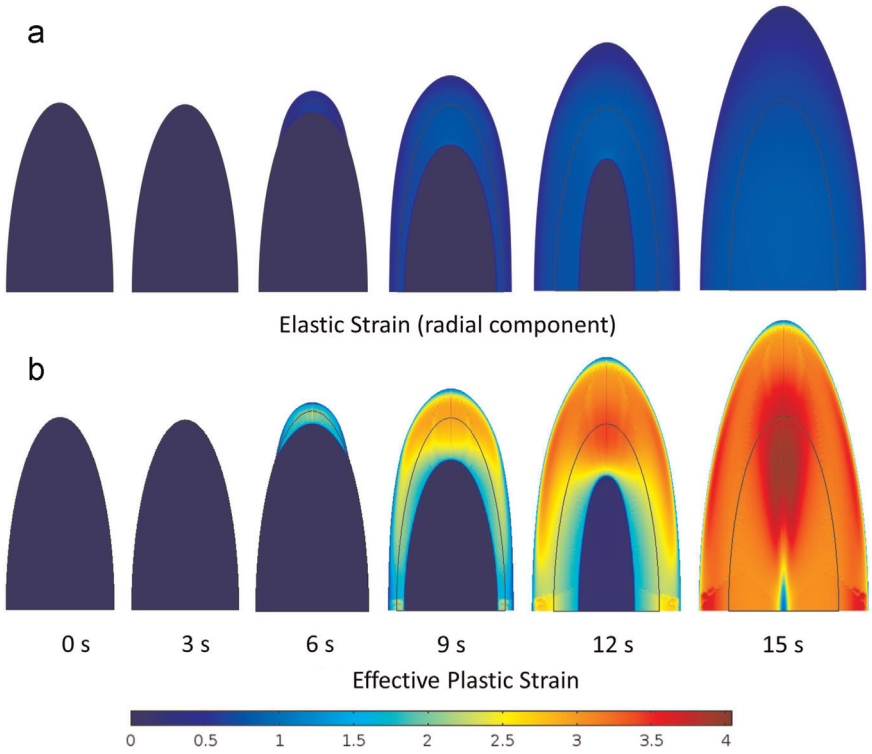

Fig. 23. Computed elastic strain (a) and effective plastic strain (b) inside the rice kernel at different puff times.

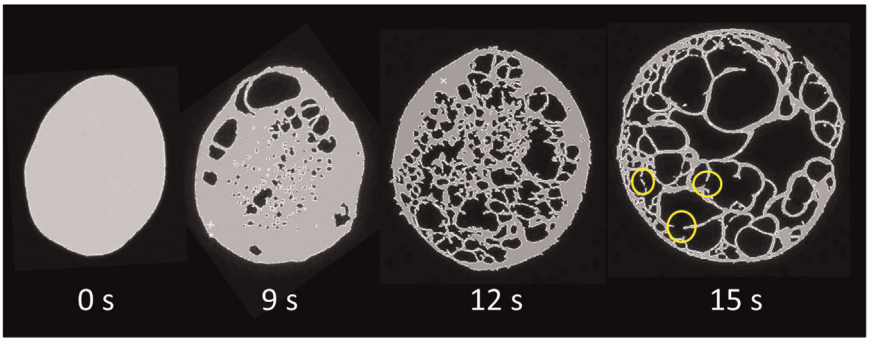

Fig. 24. Necking and pore wall rupture during rice puffing.

saturation temperature of liquid water resulting in slightly more evaporation which leads to a lower moisture in the material. Therefore, volume expansion is more sensitive to changes in the intrinsic permeability of the material compared with the final moisture content.

5.7.2. Bulk modulus in the rubbery state

Bulk modulus of starch as computed from elastic modulus in rubbery state is estimated to be 17 kPa using Eq. (64) (Fan et al., 2012; Wang et al., 2005). In the constitutive equation, it is essentially the bulk modulus that controls the expansion of the material as described in Section 2.5.2. A lower bulk modulus corresponds to a soft and compliant matrix that can deform easily. Bulk modulus values were varied within the range $\pm 50\%$ of the reference case. Fig. 26a shows the volume expansion histories with changes in the bulk modulus of the material. As is expected, a reduced bulk modulus would result in a higher expansion of the kernel. However, there is not much change in the moisture lost from the material (Fig. 26b). The flow (or transport) inside the porous medium is mainly affected by changes in the porosity due to deformation (Rakesh and Datta, 2012). The change in porosity of the material varied in the range 5.9–4.6% for -50% to $+50\%$ change in the bulk modulus indicating a very small change in porosity values. As a result, transport inside the material is not affected as much by changes in the bulk modulus, showing lack of sensitivity of moisture loss to bulk modulus variations. Therefore, more accurate values of bulk modulus may not be required for predicting moisture loss or final moisture content of the puffed kernel. However, volume change depends significantly on the value of bulk modulus chosen and thus would require accurate values.

To summarize, the choice of intrinsic permeability and bulk modulus values considerably affect the deformation of the material while moisture loss is not as sensitive to permeability and bulk modulus values.

6. Key factors affecting the rice puffing process

Several factors have been identified that affect the final expansion of the rice kernel such as (1) initial moisture content of rice, (2) puffing temperatures and (3) salt pre-treatments (Chinnaswamy and Bhattacharya, 1983; Hoke et al., 2005). Using the computational model developed above, the effects of various

processing conditions on the final volume of the puffed product are studied next to help understand the optimum conditions for puffing rice.

6.1. Initial moisture content

The initial moisture content of the rice grains at the start of the puffing process is one of the most important variables that affect expansion ratio of the kernel. An optimum moisture content is desirable since too low an initial moisture content value may cause the rice kernel to dry out much faster, thereby decreasing its ability to generate large pressures for expansion whereas, too high a moisture content would require higher energy for evaporation leading to reduced vapor generation. Also, it has been found experimentally that rice soaked to a higher moisture content in the pre-processing step before puffing develop cracks on the surface that provide channels for vapor escape during the puffing process (Murugesan and Bhattacharya, 1991). The initial moisture content of rice can be controlled during the air-drying stage in the pre-processing step. Different initial moisture content values were considered for the simulations: 0.06, 0.18, and 0.24 wet basis (wb) and compared with the reference case of 0.12 wb. The volume change of the rice kernels was quite appreciable for the range of initial moisture contents considered (Fig. 27a). The final volume of the driest sample (0.06 wb) was 40% less whereas for the wet sample (0.24 wb), the expansion was 26% more when compared with the expansion for the reference case. Also, moisture loss from the drier kernel was much higher (72%) compared with the wet sample (49%) as shown in Fig. 27b. Increased moisture loss from the drier sample is due to the reduced energy requirement for vapor generation. For the wet sample considered, the increase in expansion is lower due to higher energy requirements for evaporation at higher moisture levels. Surface cracks that develop for high moisture kernels also tend to prevent higher expansion due to vapor escape. This effect could not be captured in the modeling framework to explain the experimental observations of lower expansion for wet materials (Chinnaswamy and Bhattacharya, 1983; Murugesan and Bhattacharya, 1991).

6.2. Puffing temperatures

After moisture content, operating temperature is the next most critical factor to consider during the puffing process. If the temperatures are too low, the material may take a longer time to undergo the glassy–rubbery phase transition and would simply dry out. On the other hand, too high a value may cause the kernel to charr (or burn), together with much higher rates of moisture loss, leading to drying up the kernel (Chandrashekhar and Chattopadhyay, 1991). Consequently, less moisture will be available for internal evaporation, decreasing the final expansion ratio of the kernel. Different puffing temperatures were considered for simulation purposes: 150, 250, 300 and 350 °C. For the reference case,

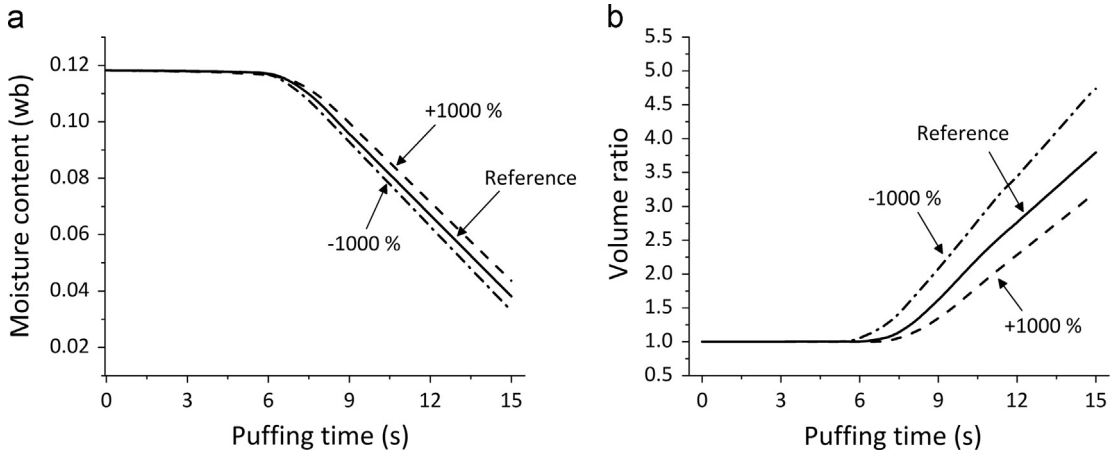

Fig. 25. Sensitivity of rice puffing process to changes in intrinsic permeability of liquid water using the total moisture loss and volume expansion as the variable of interest.

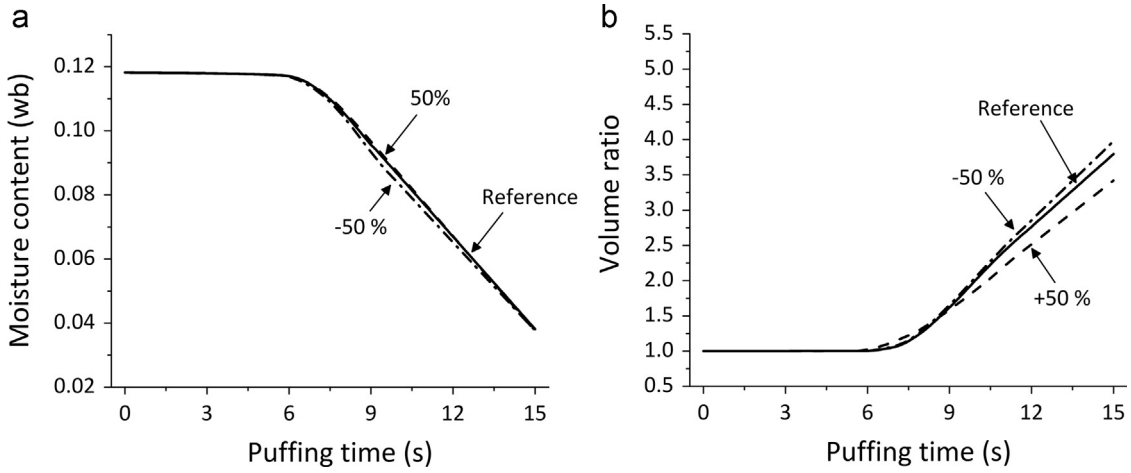

Fig. 26. Sensitivity of rice puffing process to changes in bulk modulus using the total moisture loss and volume expansion as the variable of interest.

the operating temperature was 200 °C. Fig. 28a compares the final volume expansion of the kernels for the different temperatures considered. The volume changes were higher compared with the reference case but there was no appreciable change in the volume of the puffed product between 250 °C and 350 °C. However, moisture loss from the material was high for temperatures 250–350 °C (Fig. 28b). A higher surface temperature causes earlier phase transition from glassy to rubbery state causing an earlier onset of expansion and hence more expansion. However, higher temperatures also result in rapid moisture removal from the kernel providing lesser amounts of liquid water to generate vapors in the interior which explains no significant change in the expansion ratio for the higher temperatures.

6.3. Salt pretreatments

Pretreating rice with salt during the pre-processing step significantly affects the puffing characteristics compared with untreated rice under similar puffing conditions (Mohapatra et al., 2012). Salt pretreatment is carried out by soaking parboiled rice in 2% salt solution for three days followed by subsequent drying to 10–12% moisture content (wb) (Chandrashekhar and Chattopadhyay, 1991). Salt pretreatments have been found to increase the expansion ratio by 15% (Murugesan and Bhattacharya, 1991). Literature studies have shown that addition of salt to starch lowers the glass transition temperature, T_g, of the starch–salt system. With the lowering of T_g value, salt treated rice would begin to puff early on in comparison with the untreated rice since the glassy–rubbery transition would occur at a lower temperature. Therefore, at any instant of puffing, salt-treated rice would have a higher expansion compared with untreated rice under similar puffing conditions. Also, it has been hypothesized that since salt has a higher thermal conductivity (5.7 W/m K) compared with other components, it would facilitate better heat conduction into the kernel (Gerkens and D'Arnaud, 1963), although this would need to be verified.

The modeling framework presented above is general and changes in T_g can easily be incorporated into the modeling framework without requiring any significant reformulation of the problem. Therefore, in order to study the effects of salt on puffing, simulations were run for 2% salt addition. Farahnaky et al. (2009) reported an average drop of 5 °C in T_g values per 1% of salt addition in potato and cassava starch. Based on this, the T_g value for rice starch–salt system was lowered by 10 °C. Computations were carried out with the new T_g value corresponding to 2% salt and were compared with the reference case (0% salt). Fig. 29 shows that the computed increase in expansion is ~20% and compares well with experimental values of about 15% increase reported in the literature (Murugesan and Bhattacharya, 1991). Therefore, pretreatments of rice with salt before the puffing process helps to

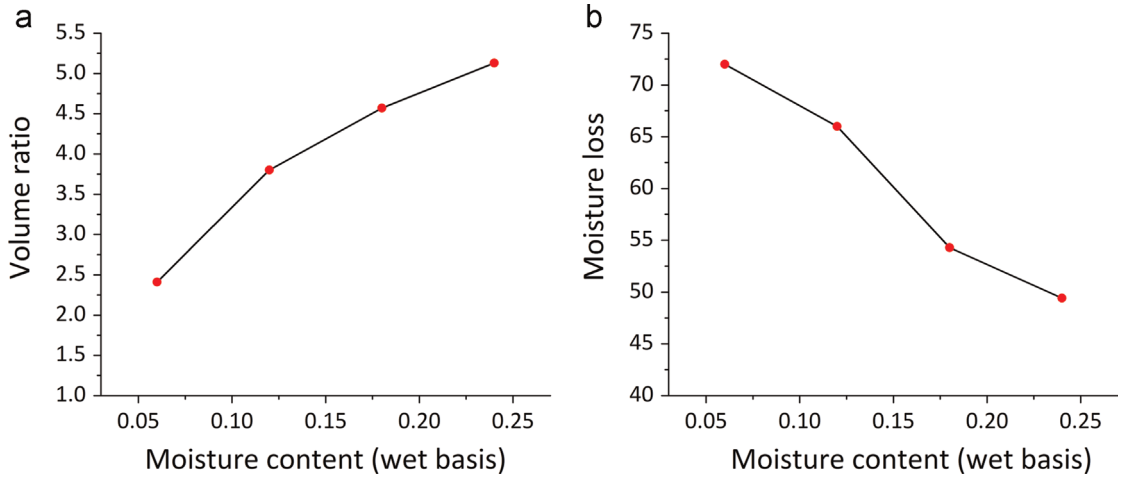

Fig. 27. Final volume and moisture loss from the puffed rice as affected by initial moisture content.

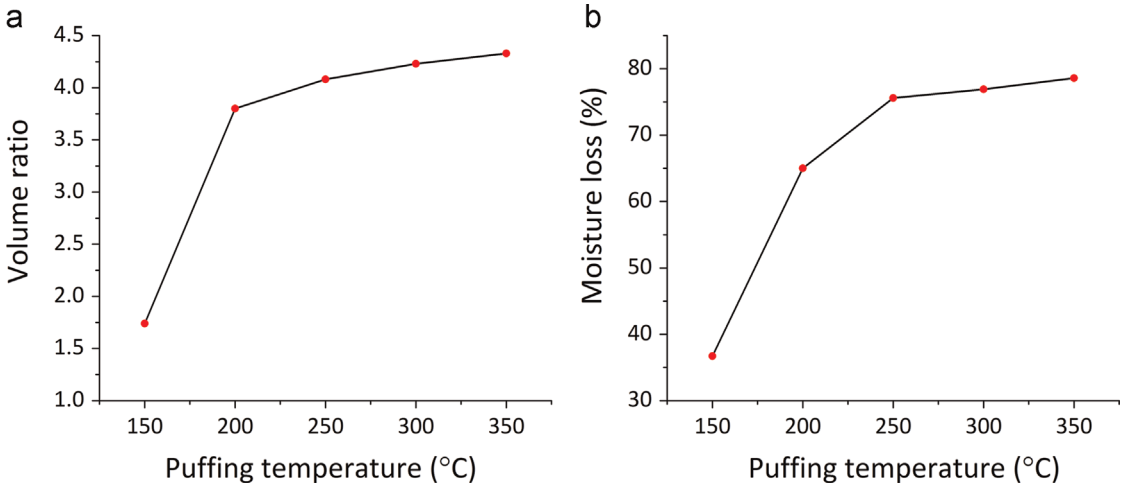

Fig. 28. Final volume and moisture loss from the puffed rice as affected by puffing temperatures.

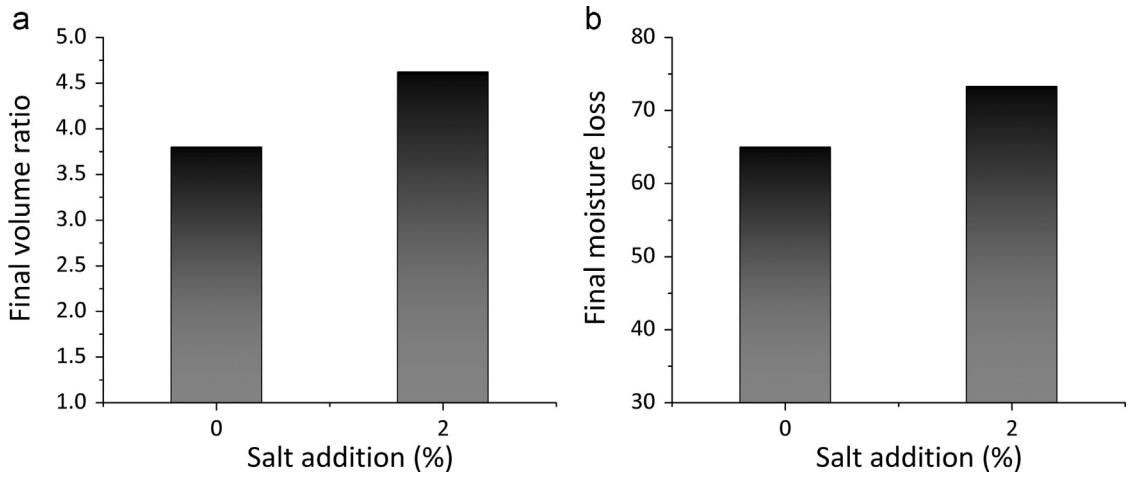

Fig. 29. Moisture loss and final volume of the puffed rice as affected by percent salt addition.

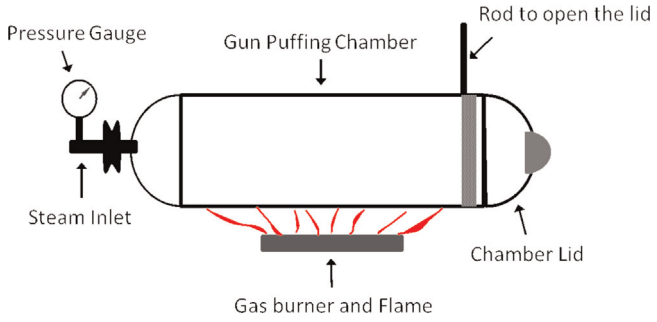

Fig. 30. Schematic showing the different components of the gun-puffing process.

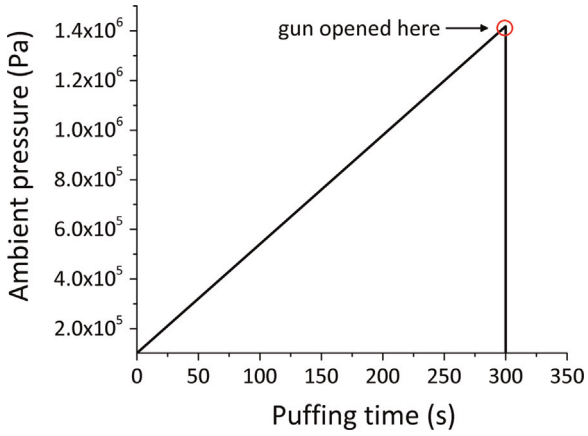

Fig. 31. Ambient pressure at the boundary of the rice kernel for the gun-puffing process.

increase the final volume of the puffed product. This is desirable since a puffed product with a higher expansion ratio provides a more crunchier mouthfeel and is an indication of a better quality product (Moraru and Kokini, 2006).

7. Model extension to gun-puffing

Gun-puffing is extensively used in the food industry for obtaining puffed cereals and grains. As applied to rice, gun-puffing typically involves rice grains in a horizontal rotating cylindrical vessel that is heated via gas burners (see Fig. 30 for schematic). A pressure gauge keeps track of the pressure that develops inside the heating chamber. Once the inside pressure reaches to approximately 8 bar, dry, super-heated steam is injected into the vessel to raise the pressure up to 14 bar and to cook the rice inside via starch gelatinization. Once the desired pressure is reached, the lid (or cover) of the cylindrical vessel is opened almost instantaneously – a very critical step. The rice kernels are shot from the gun (hence the name) and due to a sudden pressure drop, the kernels undergo a large expansion. The heating and puffing processes together last for 3–8 min (Villareal and Juliano, 1987; Hoke et al., 2005). The final expansion ratio of the puffed rice could lie anywhere between 8 and 16 (Villareal and Juliano, 1987), and it has been found experimentally that the expansion is almost uniform from all sides when compared with, for example, salt or sand assisted puffing.

7.1. Mathematical model

In this section, the mathematical model presented above for salt-assisted puffing is extended to the process of gun-puffing of rice kernels. The modeling framework is as depicted in Fig. 1. Coupled conservation equations for solid mechanics and multiphase transport (Eqs. (14), (32)–(34) and (50)), along with auxiliary equations (Eqs. (61)–(65)) described earlier, are used to solve for the key process parameters for the gun-puffing process. The most important variable of interest is the gas pressure and its gradient inside the kernel that drives the deformation. Boundary conditions for the governing equations are discussed in Section 2.4. Since there is no information about how the pressure varies inside the gun-puffing chamber, the pressure inside the chamber (and thus at the boundary of the rice kernel) was varied linearly with time from 1 atm to 14 atm for a total process time of 5 min. followed by an instantaneous pressure drop (~0.005 s) to atmospheric values to account for gun opening. The pressure at the boundary is depicted in Fig. 31. This is different from the pressure at the boundary during salt-assisted puffing (Eq. (55)) which stays at atmospheric values throughout. Required input parameters and solution methodology for the gun-puffing process were similar with salt-assisted puffing as discussed in Table 1 and Section 3, respectively.

7.2. Volume expansion

Fig. 32 shows the volume expansion history of rice shot from the gun for a gun opening time (i.e., the time to drop the pressure from 14 to 1 atm) of 0.005 s. There is relatively less expansion when the kernel is inside the gun since the ambient pressure inside the gun restricts the deformation of the kernel. However, as soon as the pressure is released (i.e., the gun is opened), expansion

happens almost instantaneously (like a spike). The computed expansion ratio before and after the process is 11.7 and agrees well with experimental expansion of 12.7 ± 2.36 for 22 varieties of rice (Villareal and Juliano, 1987). Time for pressure to drop, i.e., time to open the gun, drastically affects the final expansion. Fig. 33 shows the final volume expansion increases significantly with a decrease in pressure release time from the gun to atmospheric conditions. This is due to a larger pressure gradient (that drives the expansion) in the kernel when the gun is opened instantaneously compared to when opened slowly.

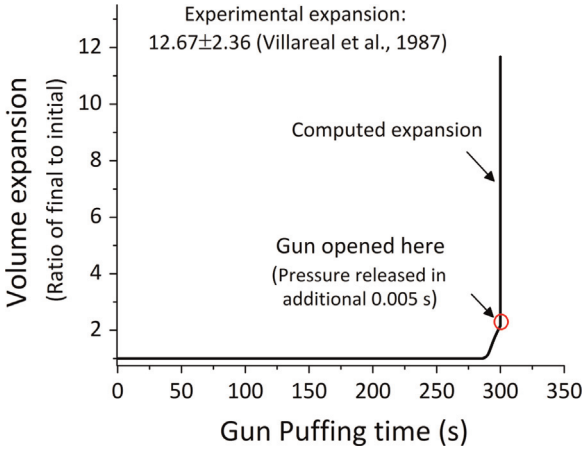

Fig. 32. Computed volume expansion history of the rice kernels after gun-puffing. Expansion ratio is computed by dividing volume at any time by volume at zero time. The pressure release time, i.e., the time for the pressure to decrease from 14 atm to 1 atm after the gun is opened, is 0.005 s.

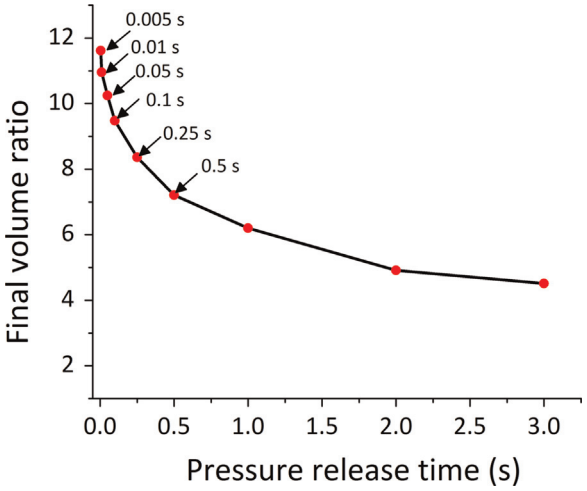

Fig. 33. Final volume ratio versus pressure release (gun-opening) time. The expansion is significant for a small gun-opening time.

7.3. Comparison with salt-assisted puffing

As was shown for salt-assisted puffing, when the temperature of the kernel increases, there is large internal evaporation resulting in pressure generation and simultaneously, the material changes from glassy to rubbery phase that then leads to puffing. On the contrary, for gun-puffing, the kernel expansion is restricted due to a higher ambient pressure at the kernel surface that reduces the gas pressure gradient and prevents significant puffing inside the gun-puffing chamber. A large part of the expansion occurs during the pressure release stage of the process where there is a sudden increase in the gas pressure gradient allowing for much higher expansion (computed expansion ratio of 11.7) compared with salt-assisted puffing (computed expansion ratio of 3.8). Moreover, the volumetric expansion of the kernel is uniform from all sides (Fig. 34) in gun-puffing compared with salt-assisted puffing for which the expansion begins from the tip of the kernel (Fig. 12). This is because during gun-puffing, the kernels are slowly heated and there is enough time for the rice kernels to attain uniform temperatures within. Consequently, the entire kernel undergoes glass transition to the rubbery state and therefore expands uniformly. This is in contrast to salt-assisted puffing for which both glassy and rubbery states co-exist inside the kernel leading to non-uniform expansion (which begins from the tip). It is probably due to higher and a more uniform expansion that gun-puffing is the preferred choice for making puffed-breakfast cereals by the food industry.

8. Conclusions

A fully coupled model for multiphase transport, large deformation and phase transition during salt-assisted puffing of rice kernels was developed and solved using finite elements along with extensive experimental validation. A detailed understanding of flow and deformation during rice puffing, such as rapid evaporation, glass transition, pressure development, large volumetric expansion and the coupling between different physics, was studied. A parametric sensitivity analysis was carried out with respect to some important input parameters followed by studying some key factors that affect the puffing process critically. Finally, the modeling framework was successfully extended to understand the

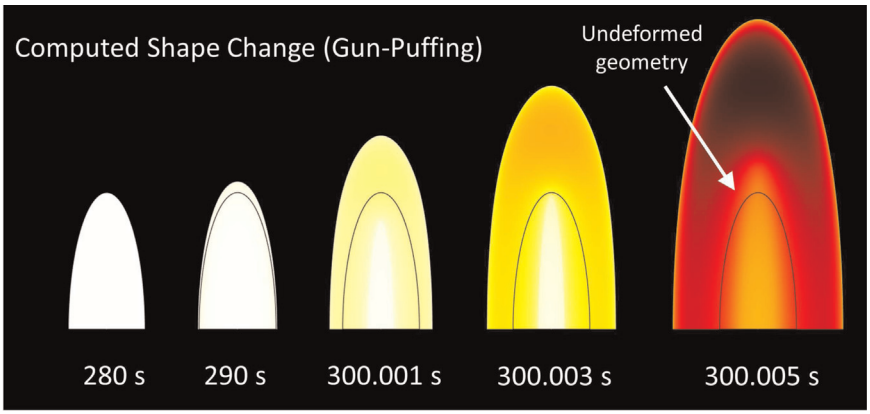

Fig. 34. Computed shape changes for gun-puffed rice. The expansion is more uniform for gun-puffed rice compared with salt-assisted puffing (see Fig. 12 for comparison).

process of gun-puffing (a completely different puffing process). From a quality standpoint, it is desired to have a higher volume expansion of the puffed product.

Key conclusions of this work are summarized as follows: (1) the model accurately predicts the experimental volume expansion ratio, dimension changes, moisture loss, shape evolution and gas porosity during salt-assisted puffing of rice kernels. (2) High temperatures are required to cause rapid evaporation of water in order to generate large pressures and produce glassy–rubbery phase transition to make the material soft and easily deformable. (3) The rice grain starts to puff from the tip where it becomes rubbery first and the expansion front moves inwards eventually causing the entire kernel to puff from the core. (4) Large pressures are developed in the glassy regions that are subsequently released when the material transitions to the rubbery state and puffs. (5) Peak tensile stress follows pressure development inside the kernel and has a strong dependency on the state of the material (rubbery or glassy). (6) While volume expansion is particularly sensitive to bulk modulus and intrinsic permeability, moisture loss is not sensitive to the same. (7) An optimum initial moisture content value of the rice kernel is needed to get a higher expansion ratio. (8) The expansion of the kernels is low for low temperature puffing whereas, at very high temperatures, the material dries out and the final expansion is not significantly higher compared with puffing at intermediate temperatures. (9) Salt pretreatment of rice before puffing helps achieve a higher expansion due to lowering of the glass transition temperature and an early onset of glassy–rubbery phase transition. (10) Gun-puffing results in a higher and uniform expansion of the kernel compared to salt-assisted puffing and the gun-puffed product is highly sensitive to the pressure release time from the gun-puffing chamber.

Nomenclature

Symbol	Description	Units
$\mathbf{B}$	left Cauchy Green deformation tensor	
c	concentration	kg/m^{-3}
C_p	specific heat capacity	J/kg K
C_g	molar density	$kmol/m^3$
$\mathbf{C}$	right Cauchy Green deformation tensor	
$D_{eff,g}$	vapor diffusivity in air	m^2/s
$D_{w,cap}$	capillary diffusivity	m^2/s
E	elastic modulus	N/m^2
$\mathbf{E}$	Green–Lagrange strain tensor	
F	Yield function	
$\mathbf{F}$	deformation tensor	
h_t	heat transfer coefficient	W/m^2 K
h_m	mass transfer coefficient	m/s
$\dot{I}$	rate of evaporation	kg/m^3 s
$\mathbf{I}$	Identity tensor	
J	Jacobian	
$k_{in,i}$	intrinsic permeability	m^2
$k_{r,i}$	relative permeability of component i	
K_{evap}	evaporation rate constant	1/s
m	overall mass fraction	
M	moisture content (dry basis)	kg water/kg dry solid
M_a, M_v	molecular weight of air and vapor	
$\overrightarrow{N}$	unit normal	
p	pressure	Pa
p_c	capillary pressure of water	Pa
Q	microwave source term	W/m^3
r	radius	m
R	universal gas constant	J/kmol K
S_i	saturation of a fluid phase, i	
$\mathbf{S}^{''}$	Piola–Kirchoff stress tensor	Pa
t	time	s
$\boldsymbol{\tau}$	Kirchoff stress deviator	Pa
T	temperature	°C
$\overline{u}$	displacement	m
$\overline{v}$	velocity	m/s
x_a, x_v	mole fraction of air and vapor in gas phase	
V	volume	m^3
W	strain energy function	J
$\overline{x}$	coordinates in spatial frame	m
$\overline{X}$	coordinates in material frame	m

Greek symbols

ρ	density	kg/m^3
λ	latent heat of vaporization	J/kg
ω_a, ω_v	mass fraction of air and vapor	
α	effective plastic strain	
ϕ	porosity	
μ	shear modulus	Pa
μ_i	dynamic viscosity of phase i	Pa s
λ	plastic multiplier	
μ_0	permeability of free space	$4\pi \times 10^{-7}$ H/m
ν	Poisson's ratio	
$\overline{\boldsymbol{\sigma}}$	stress	Pa
σ_0	yield stress	Pa

Subscripts

amb	ambient
a, f, g, s, v, w	air, fluid, gas, solid, vapor, water
c	capillary
el	elastic
eff	effective
eq	equilibrium
f	fracture
G	ground (stationary observer)
i	*i*th phase
M	moisture
p	plastic
0	at time $t=0$
surf	surface

Acknowledgments

This project is supported by Agriculture and Food Research Initiative Competitive Grant no. 2009-65503-05800 from the USDA National Institute of Food and Agriculture. The authors also wish to thank Mark Riccio of Cornell University Biotechnology Resource Center (BRC) for his help with micro-CT experiments.

References

Achanta, S., 1995. Moisture transport in shrinking gels during drying (Ph.D. thesis). Purdue University, Indiana, United States.

Alavi, S.H., Rizvi, S.S.H., Harriott, P., 2003a. Process dynamics of starch-based microcellular foams produced by supercritical fluid extrusion. I: model development. Food Res. Int. 36 (4), 309–319.
Alavi, S.H., Rizvi, S.S.H., Harriott, P., 2003b. Process dynamics of starch-based microcellular foams produced by supercritical fluid extrusion. II: numerical simulation and experimental evaluation. Food Res. Int. 36 (4), 321–330.
Arefmanesh, A., Advani, S.G., Michaelides, E.E., 1990. A numerical study of bubble growth during low pressure structural foam molding process. Polym. Eng. Sci. 30 (20), 1331–1338.
Bear, J., 1972. Dynamics of Fluids in Porous Media. American Elsevier Publishing Company, New York.
Bird, R.B., Stewart, W.E., Lightfoot, E.N., 2001. Transport Phenomena 2nd edition. John Wiley Sons Inc, New York, USA.
Bostwick, K.S., Riccio, M.L., Humphries, J.M., 2012. Massive, solidified bone in the wing of a volant courting bird. Biol. Lett. 8, 760–763.
Briffaz, A., Mestres, C., Escoute, J., Lartaud, M., Dornier, M., 2012. Starch gelatinization distribution and peripheral cell disruption in cooking rice grains monitored by microscopy. J. Cereal Sci. 56, 699–705.
Chandrashekhar, P.R., Chattopadhyay, P.K., 1991. Rice puffing in relation to its varietal characteristics and processing conditions. J. Food Process Eng. 14, 261–277.
Chinnaswamy, R., Bhattacharya, K.R., 1983. Studies on expanded rice. Optimal processing condition. Journal of Food Science 48, 1604–1608.
Chiotellis, E., Campbel, G.M., 2003. Proving of bread dough I: modeling the evolution of the bubble size distribution. Trans. IChemE, Part C, Food Bioprod. Process. 81, 194–206.
Choi, Y., Okos, M.R., 1986. Thermal properties of liquid foods—review. In: Okos, M.R. (Ed.), Physical and Chemical Properties of Food. American Society of Agricultural Engineers, St. Joseph, MI, USA.
Chung, H.J., Lee, E.J., Lim, S.T., 2002. Comparison in glass transition and enthalpy relaxation between native and gelatinized starches. Carbohydr. Polym. 48, 287–298.
Das, H., 2005. Food Processing Operation Analysis, 1st ed. Asian Books Private Limited, New Delhi.
Deshlahra, P., Mehra, A., Ghosal, D., 2009. Evolution of bubble size distribution in baked foods. J. Food Eng. 93, 192–199.
Dhall, A., Datta, A.K., 2011. Transport in deformable food materials: a poromechanics approach. Chem. Eng. Sci. 66 (24), 6482–6497.
Dupaix, R.B., Boyce, M.C., 2007. Constitutive modeling of the finite strain behavior of amorphous polymers in and above the glass transition. Mechanics of Materials 39, 39–52.
Elshereef, R., Vlachopoulos, J., Elkamel, A., 2010. Comparison and analysis of bubble growth and foam formation models. Eng. Comput. 27 (3), 387–408.
Farahnaky, A., Farhat, I.A., Mitchell, J.R., Hill, S.E., 2009. The effect of sodium chloride on the glass transition of potato and cassava starch at low moisture contents. Food Hydrocoll. 23, 1483–1487.
Fan, X., Meng, Z., Zhou, J., Xu, W., Xiang, H., Yang, G., 2012. Investigation of bubble growth in extrusion expansion of cornstarch with CFD method. Int. J. Food Eng. 8 (2), 13.
Fan, J.T., Mitchell, J.R., Blanshard, J.M.V., 1999. A model for the oven rise of dough during baking. J. Food Eng. 41 (2), 69–77.
Fan, J., Mitchell, J.R., Blanchard, J., 1994. A computer simulation of the dynamics of bubble growth and shrinkage during extrudate expansion. J. Food Eng. 23, 337–356.
Fukuoka, M., Mihori, T., Watanabe, H., 2000. MRI observation and mathematical model simulation of water migration in wheat flour dough during boiling. J. Food Sci. 65, 1343–1348.
Genovese, D.B., Rao, M.A., 2003. Vane yield stress of starch dispersions. J. Food Sci. 68, 2295–2301.
Gerkens, D.R., D'Arnaud, 1963. U.S. Patent 3,076,711. In: Lachmann, A. (Ed.). 1969: Snacks and Fried Products. Noyes Development Corp., Park Ridge, NJ, p. 149.
Gulati, T., Datta, A.K., 2013. Enabling computer-aided food process engineering: property estimation equations for transport phenomena-based models. J. Food Eng. 116, 483–504.
Guraya, H.S., Toledo, R.T., 1994. Volume expansion during hot air puffing of a fat-free starch-based snack. J. Food Sci. 59 (3), 641–643.
Hailemariam, L., Okos, M., Campanella, O., 2007. A mathematical model for the isothermal growth of bubbles in wheat dough. J. Food Eng. 82 (4), 466–477.
Halder, A., Dhall, A., Datta, A.K., 2007. An improved, easily implementable, porous media based model for deep-fat frying—Part I: model development and input parameters. Food Bioprod. Process. 85 (C3), 209–219.
Halder, A., Datta, A.K., Spanswick, R.M., 2011. Water transport in cellular tissues during thermal processing. AIChE J. 57, 2574–2588.
Hoke, K., Houska, M., Jirina, P., Gabrovska, D., Vaculova, K., Paulickova, I., 2007. Optimization of puffing naked barley. J. Food Eng. 80, 1016–1022.
Holzapfel, G.A., 2000. Nonlinear Solid Mechanics. Wiley, Chichester, UK.
Hoke, K., Housova, J., Houska, M., 2005. Optimum conditions of rice puffing. Czech J. Food Sci. 23 (1), 1–11.
Hoseney, R.C., Zeleznak, K., Abdelrahman, A., 1983. Mechanism of popcorn popping. J. Cereal Sci. 1 (1), 43–52.
Joshi, N.D., Mohapatra, D., Joshi, D.C., Sutar, R.F., 2014. Puffing characteristics of parboiled milled rice in a domestic convective-microwave oven and process optimization. Food Bioprocess Technol. 7, 1678–1688.
Katekawa, M.E., Silva, M.A., 2006. A review of drying models including shrinkage effects. Dry. Technol. 24 (1), 5–20.
Kim, B.K., Lee, S.B., Lee, J., Cho, S.H., Park, H.M., Yeom, S.H., Park, S.H., 2012. A comparison among neo-Hookean model, Mooney–Rivlin model, and Ogden model for chloroprene rubber. Int. J. Precis. Eng. Manuf. 13 (5), 759–764.
Kokini, J.L., Chang, C.N., Lai, L.S., 1992. The role of rheological properties on extrudate expansion. In: Kokini, J.L., Ho, C.-T., Karwe, M.V. (Eds.), Food Extrusion Science and Technology. Marcel Dekker Inc., New York, NY, pp. 631–653.
Kong, I., Shanks, R., 2012. Thermoplastic starch. In: El-Sonbati, A.Z. (Ed.), Thermoplastic Elastomers.
Lewis, M., 1987. Physical Properties of Foods and Food Processing Systems. VCH, Deerfield Beach, FL.
Lewis, R.W., Schrefler, B.A., 1987. The Finite Element Method in the Deformation and Consolidation of Porous Media. John Wiley & Sons Ltd, West Sussex, England.
Lue, S., Hsieh, F., Huff, H.E., 1991. Extrusion cooking of corn meal and sugar beet fiber: effects on expansion properties, starch gelatinization, and dietary fiber content. Cereal Chem. 68 (3), 227–234.
McCabe, W., Smith, J., Harriott, P., 2005. Unit Operations of Chemical Engineering, seventh ed. McGraw-Hill, Boston, MA.
Maisont, S., Narkrugsa, W., 2010. Effects of salt, moisture content and microwave power on puffing qualities of puffed rice. Kasetsart J. 44, 251–261.
Mayor, L., Sereno, A.M., 2004. Modelling shrinkage during convective drying of food materials: a review. J. Food Eng. 61 (3), 373–386.
Mohapatra, M.A., Kumar, A., Das, S.K., 2012. Mixing characteristics of rice by tracer technique in an agitated cylindrical preconditoner developed for puffed rice production system. J. Food Process Eng. 35, 784–791.
Moldrup, P., Olesen, T., Yoshikawa, S., Komatsu, T., Rolston, D.E., 2005. Predictive–descriptive models for gas and solute diffusion coefficients in variably saturated porous media coupled to pore-size distribution: I. Gas diffusivity in repacked soil. Soil Sci. 170 (11), 843–853.
Moraru, C.I., Kokini, J.L., 2006. Nucleation and expansion during extrusion and microwave heating of cereal foods. Compr. Rev. Food Sci. Food Saf. 2 (4), 147–165.
Moscicki, L., 2011. Snack pellets. Extrus. Cook. Techn., 81–89.
Murthy, V.K., Das, A.K., Raghavarao, K.S.M.S., 2009. Modelling of heat and mass transfer during puffing and popping of grains by fluidization. In: CSIR Workshop: Advances and Applications of Mathematical Modelling, 23–25 May, Bangalore, India.
Murugesan, G., Bhattacharya, K.B., 1991. Effect of some pre-treatment on popping expansion of rice. J. Cereal Sci. 13, 85–92.
Nath, A., Chattopadhyay, P.K., Majumdar, G.C., 2007. High temperature short time air puffed ready-to-eat (RTE) potato snacks: process parameter optimization. J. Food Eng. 80 (3), 770–780.
Niamnuy, C., Devahastin, S., Soponronnari, S., Raghavan, V.G.S., 2008. Modeling coupled transport phenomena and mechanical deformation of shrimp during drying in a jet spouted bed dryer. Chemical Engineering Science 63, 5503–5512.
Nicolas, V., Salagnac, P., Glouannec, P., Ploteau, J.P., Jury, V., Boillereaux, L., 2014. Modelling heat and mass transfer in deformable porous media: application to bread baking. J. Food Eng. 130, 23–35.
Norton, A.D., Greenwood, R.W., Noble, I., Cox, P.W., 2011. Hot air expansion of potato starch pellets with different water contents and salt concentrations. J. Food Eng. 105 (1), 119–127.
Perez, J.H., Tanaka, F., Uchino, T., 2012. Modeling of mass transfer and initiation of hygroscopically induced cracks in rice grains in a thermally controlled soaking condition: with dependency of diffusion coefficient to moisture content and temperature—a 3D finite element approach. J. Food Eng. 111, 519–527.
Rakesh, V., Datta, A.K., 2012. Transport in deformable hygroscopic porous media during microwave puffing. AIChE J. 59 (1), 33–45.
Rakesh, V., Datta, A.K., 2011. Microwave puffing: determination of optimal conditions using a coupled multiphase porous media-large deformation model. J. Food Eng. 107 (2), 152–163.
Ressing, H., Ressing, M., Durance, T., 2007. Modeling the mechanisms of dough puffing during vacuum microwave drying using the finite element method. Journal of Food Engineering 82 (4), 498–508.
Richeton, J., Ahzi, S., Vecchio, K.S., Jiang, F.C., Makardi, A., 2007. Modeling and validation of the large deformation inelastic response of amorphous polymers over a wide range of temperatures and strain rates. Int. J. Solids Struct. 44, 7938–7954.
Schwartzberg, H.G., Wu, J.P.C., Nussinovitch, A., Mugerwa, J., 1995. Modelling deformation and flow during vapor-induced puffing. J. Food Eng. 25 (3), 329–372.
Shah, P., Campbel, G.M., McKee, S.L., Riely, C.D., 1998. Proving of bread dough: modeling the growth of individual bubbles. Trans. IChemE, Part C, Food Bioprod. Process. 76, 73–79.
Shi, X., Datta, A.K., Mukherjee, Y., 1998. Thermal stresses from large volumetric expansion during freezing of biomaterials. J. Biomech. Eng. Trans. ASME 120 (6), 720–726.
Shitanda, D., Nishiyama, Y., Koide, S., 2002. Compressive strength properties of rough rice considering variation of contact area. Journal of Food Engineering 53 (1), 53–58.
Simo, J.C., Hughes, T.J.R., 1998. Computational Inelasticity. Springer-Verlag Inc., New York, NY.
Simsrisakul, M., 1991. Important factors affecting puffing quality of paddy and properties of puffed rice flour (M.Sc. thesis). Chulalongkorn University, Bangkok.
Srivastava, V., Chester, S.A., Ames, N.M., Anand, L., 2010. A thermomechanically-coupled large-deformation theory for amorphous polymers in a temperature range which spans their glass transition. Int. J. Plast. 26, 1138–1182.
Taki, K., Tabata, K., Kihara, S., Ohshima, M., 2006. Bubble coalescence in foaming process of polymers. Polym. Eng. Sci. 46 (5), 680–690.

Tanikawa, W., Shimamoto, T., 2009. Comparison of Klinkenberg-corrected gas permeability and water permeability in sedimentary rocks. Int. J. Rock Mech. Min. Sci. 46 (2), 229–238.
van der Sman, R.G.M., Broeze, J., 2013. Structuring of indirectly expanded snacks based on potato ingredients: a review. J. Food Eng. 114, 413–425.
Varnalis, A.I., Brennan, J.G., MacDougall, D.B., Gilmour, S.G., 2004. Optimisation of high temperature puffing of potato cubes using response surface methodology. J. Food Eng. 61 (2), 153–163.
van der Lijn, J., 1976. Simulation of heat and mass-transfer in spray drying (Ph.D. thesis). Agricultural University of Wageningen, The Netherlands, pp. 77–80.
van der Sman, R.G.M., Meinders, M.B.J., 2011. Prediction of the state diagram of starch water mixtures using the Flory–Huggins Free Volume theory. Soft Matter 7 (2), 429–442.
Villareal, CP., Juliano, BO., 1987. Varietal differences in quality characteristics of puffed rices. J. Cereal Chem 64 (4), 337–342.
Warning, A., Verboven, P., Nicolai, B., van Dalen, G., Datta, A.K., 2014. Computation of mass transport properties of apple and rice from X-ray microtomography images. Innov. Food Sci. Emerg. Technol. 24, 14–27.
Wang, L.J., Ganjyal, G.M., Jones, D.D., Weller, C.L., Hanna, W.L., 2005. Modeling of bubble growth dynamics and non-isothermal expansion in starch-based foams during extrusion. Adv. Polym. Technol. 24 (1), 29–45.
Willard, M.J., 1976. Method for making expanded potato based snack products. US Patent 3,997,684.
Wu, P.J., Schwartzberg, H.G., 1994. Determination of vapor pressure in vapor induced puffing. AIChE J. 40, 160–165.
Yang, H., Sakai, N., Watanabe, M., 2001. Drying model with non-isotropic shrinkage deformation undergoing simultaneous heat and mass transfer. Dry. Technol. 19 (7), 1441–1460.
Yue, P., Feng, J.J., Bertelo, C.A., Hu, H.H., 2007. An arbitrary Lagrangian–Eulerian method for simulating bubble growth in polymer foaming. J. Comput. Phys. 226 (2), 2229–2249.
Zhang, J., Datta, AK., Mukherjee, S., 2005. Transport processes and large deformation during baking of bread. AIChE Journal 51 (9), 2569–2580.